DCE23

5th DOCTORAL CONGRESS IN ENGINEERING

Book of Abstracts

DCE23 - Symposium on Biomedical Engineering

U.PORTO
FEUP FACULDADE DE ENGENHARIA
UNIVERSIDADE DO PORTO

DCE 23 5th DOCTORAL CONGRESS IN ENGINEERING

Book of Abstracts

of the

Symposium on Biomedical Engineering

Editors:
Tiago Pousa Ribeiro, Fernando Jorge Monteiro, Maria Pia Ferraz

Porto
June 2023

OUR SILVER SPONSORS

This volume contains the peer reviewed and accepted abstracts, presented at the Symposium on Biomedical Engineering, of the 5th Doctoral Congress in Engineering – DCE23, held at FEUP-U.Porto, Porto, Portugal, between June 15th and 16th, 2023.

Title: Book of Abstracts of DCE'23 Symposium on Biomedical Engineering

Edited by Tiago Sousa Ribeiro, Fernando Jorge Monteiro, Maria Pia Ferraz

Published by: FEUP Edições

Digital version Symposium on Biomedical Engineering – DCE 2023 (up.pt)

First edition June 2023

ISBN. 978-972-752-312-2

OUR BRONZE SPONSORS

UNIVERSIDADES

WELCOME

Welcome

It is our great honor to welcome you to the Symposium on Biomedical Engineering, integrated into the Fifth Doctoral Congress in Engineering (DCE), hosted at FEUP, Porto, Portugal on the 15th and 16th of June, 2023.

The Symposium on Biomedical Engineering aims to provide knowledge transfer between FEUP and other national and international participants, encouraging them to present their ongoing research and promote networking. The event is mainly focused on the participation of doctoral students, yet master students are also welcome to participate.

Through a multidisciplinary and informal atmosphere, the meeting will create a great environment for discussing the latest developments on topics such as: Bioimaging and radiation; Biomedical devices; Biomechanics; BioRobotics; Biomaterials and Artificial Organs; Neuroscience/Neuroengineering; Bioinformatics; Computer Vision; Computer Modelling; Information Management and Hospital Equipment.

These meeting will be held in an informal environment, allowing close and detailed discussions among participants. We hope you will enjoy a pleasant meeting.

Porto, June 2023

Symposium Organizing Committee

CONTENTS

Contents

COMMITTEES

Organizing Committee

Chair: Fernando Jorge Monteiro| FEUP

Co-Chair: Maria Pia Ferraz | FEUP

Tiago Pousa Ribeiro| i3S/FEUP

Scientific Committee

Chair: Fernando Jorge Monteiro | FEUP

Co-Chair: Maria Pia Ferraz | FEUP

Christiane Salgado | i3S

Cláudia Monteiro| i3S

Joana Barros | i3S

Marta de Sousa Laranjeira| i3S

Ana Mendonça| FEUP

João Miguel Velhote| FEUP

João Paulo Cunha| FEUP

Joaquim Mendes| FEUP

Maria Ascenção Lopes| FEUP

Symposium Programme – June 15th

Time	Event	Location
8:00	Welcoming	Reception
9:00	Opening Session	Auditorium
9:30	Industry Keynote lecture	Auditorium
10:00	Round table	Auditorium
11:00	Coffee-break	Coffee lounge
11:30	Plenary Session	Auditorium
13:00	Lunch	Coffee lounge
14:00	Poster Session	Building B
15:00	Selected Oral Presentations	B021
16:30	Coffee-break	Coffee lounge
17:00	Selected Oral Presentations	B021

Symposium Programme – June 16th

Time	Event	Location
8:00	Welcoming	Reception
9:00	Selected Oral Presentations	B021
10:30	Coffee-break	Coffee lounge
11:00	Selected Oral Presentations	B021
13:00	Lunch + Poster Session	Coffee lounge
14:30	Award Ceremony	Auditorium
15:30	Keynote Lecture	Auditorium
16:00	Closing Session	Auditorium
16:30	Cocktail/Porto d'Honra	Coffee lounge

Oral Communications to be presented in the Symposium

Selected Talk 01

The effect of ultrasonication and high shear mixing in MoS2 and WS2 exfoliation for biomedical applications MoS2 and WS2 exfoliation for biomedical applications

Filipa A. L. S. Silva, Bruno Freitas, Hui-Ping Chang, José R. Fernandes, Fernão D. Magalhães, Susana G. Santos, Jean-Anne Incorvia, Artur M. Pinto

Selected Talk 02

Fast-forward on skin wound resolution with antimicrobial and pro-angiogenic peptides: is covalent conjugation to norbornene-chitosan nanoparticles worth it?

Pedro M. Alves, Diana R. Fonseca, Sílvia J. Bidarra, Ana Gomes, Cristina C. Barrias, Paula Gomes, M. Cristina L. Martins

Selected Talk 03

"In vitro" characterization of different formulations of hydrogel-based dressings

Maria Gomes, Bruno Colaço, Pedro Gomes, Joana Barros

Selected Talk 04

A multifunctional gelatin-based gel for periodontal regeneration in dogs

Laura Pinho, André Queirós, Joana Marto, Catarina Santos, Bruno Colaço, Maria Helena Fernandes

Selected Talk 05

Development of functionalized nanoparticles with an innovative microfluidics one-pot setup: proof of concept with chitosan and antimicrobial peptides for Helicobacter pylori management

Diana R. Fonseca, Pedro M. Alves, Estrela Neto, Beatriz Custódio, Sofia Guimarães, Marco Martins, Ana Gomes, Paula Gomes, Ruben Pereira, Paulo Freitas, Paula Parreira, M. Cristina L. Martins

Selected Talk 06

MRI-based radiomics for assessment of the infrapatellar fat pad's influence on patellofemoral pain

Inês R. Campos, Rianne A. van der Heijden, Edwin H.G. Oei, Marienke van Middelkoop, Stefan Klein, Jaime S. Cardoso, Jukka Hirvasniemi

Selected Talk 07

Phase Analysis of Back-Scattering Signals from Optical Fiber Tweezers for Bioparticles Detection and Differentiation

Beatriz Barros, João Paulo Cunha

Selected Talk 08

Functionalization with cannabidiol increases the BBB targeting capacity of small-sized lipid nanocapsules

Alexandre Pérez-López, Juan Aparicio-Blanco, Cristina Martín-Sabroso, Juan F González-Matilla, Ana I Torres Suárez

Selected Talk 9

Poly(lactic-co-glycolic acid)/graphene nanoparticles for combined drug delivery and cancer phototherapy

Bruno Freitas, Filipa A. L. S. Silva, José Ramiro Fernandes, Susana G. Santos, Maria J. Oliveira, Joana Paredes, Fernão D. Magalhães, Artur M. Pinto

Selected Talk 10

Combining 3D Models of Anatomical and Thermal Images

Catarina Lopes, Adelio Vilaca, Cristina Santos, Joaquim Mendes

Selected Talk 11

Muscle coactivation analysis for neuromuscular control assessment of lower limb stretch-shortening cycle

Carlos Rodrigues, Miguel Correia, João Abrantes, Marco Benedetti, Jurandir Nadal

40The effect of ultrasonication and high shear mixing in MoS_2 and WS_2 exfoliation for biomedical applications

Filipa A. L. S. Silva[1,2,3,4], Bruno Freitas[1,2,3,4], Hui-Ping Chang[5], José R. Fernandes[6,7], Fernão D. Magalhães[1,2], Susana G. Santos[3,4], Jean-Anne Incorvia[5], Artur M. Pinto[1, 2, 3, 4,*]

[1]LEPABE - Laboratory for Process Engineering, Environment, Biotechnology and Energy, Faculdade de Engenharia, Universidade do Porto, Portugal

[2]ALiCE - Associate Laboratory in Chemical Engineering, Faculdade de Engenharia, Universidade do Porto, Portugal

[3]i3S - Instituto de Investigação e Inovação em Saúde, Universidade do Porto, Portugal

[4]INEB - Instituto de Engenharia Biomédica, Universidade do Porto, Portugal

[5]Department of Electrical and Computer Engineering, University of Texas at Austin

[6]CQVR – Centro de Química Vila Real, Universidade de Trás-os-Montes e Alto Douro, Portugal

[7]Physical Department, University of Trás-os-Montes and Alto Douro, Vila Real, Portugal

* Correspondence: arturp@fe.up.pt

Author Keywords: 2D nanomaterials, transition metal dichalcogenides, liquid-based exfoliation, photothermal therapy.

Introduction: Two-dimensional transition metal dichalcogenides (TMDC), such as MoS_2 and WS_2, have been explored in the biomedical field, owing to their structural, optical and electronic properties. These materials possess high absorption in near-infrared (NIR) region, high surface area and biocompatibility, which make them excellent candidates as photothermal therapy (PTT) and drug delivery agents. [1] PTT is a targeted, non-invasive treatment based on the principle of converting near infrared (NIR) light energy into heat, leading to hyperthermia (HT), and ultimately inducing cancer cell death through mild temperature elevation (39–45°C). Above 60°C, cell necrosis occurs through thermal-ablation treatment modality. [2]

Monolayered TMDC are mainly produced from bulk materials by liquid-based exfoliation methods assisted by shock waves generated by ultrasonication that allow to break the inter-layer van der Waals bonds between materials layers, facilitating the intercalation of the exfoliation agents. [3] However, sonication is not suitable for scaling to industrial production levels, due to the long processing time and high energy consumption. As alternative, high shear exfoliation has been explored using shear forces as tool to separate sheets. [3] This technique was recently demonstrated as a facile and scalable production method, successfully applied in graphene production. [4] However, high shear exfoliation has not been fully explored for other 2DnMat. Having this in mind, we explored the effect of both ultrasonication and high shear exfoliation in MoS_2 and WS_2 exfoliation.

Methods: MoS_2 and WS_2 were produced following polyvinylpyrrolidone(PVP)-assisted liquid phase exfoliation. After, solutions were placed in contact with an ultrasounds probe (US) or mixed with an ultraturrax (UT) for 5 h in an ice bath. After washing, materials photoproperties were evaluated by measuring the absorbance spectra (200-850 nm) in a UV-Vis spectrophotometer and measuring the temperature increase after NIR irradiation. WS_2 and MoS_2 produced by US and UT were irradiated with a LED source of 812 nm (150 mW cm^{-2}) and temperature increase recorded with a thermocouple. Particles size and water stability were also analyzed by using a Zetasizer.

Results and discussion: Heating curves revealed a higher temperature increase of the samples produced by US when compared to the materials produced by UT. After 30 min irradiating, 1 mg mL^{-1} MoS_2 US reached 47.9 °C, while MoS_2 UT increased temperature solution to 46.5 °C, corresponding to a temperature increment 1.4 °C lower. The same time of irradiation (30 min) caused a temperature increase to 45.8 °C in WS_2 US (1 mg mL^{-1}), which was 4.1°C higher than WS_2 UT that reached only 41.7 °C. Materials UV-Visible absorbance spectra revealed higher absorbance in NIR region (812 nm) for WS_2 and MoS_2 US comparing with UT samples. MoS_2 US showed a 4-fold increment in NIR absorbance when compared with MoS_2 UT. WS_2 US spectra showed a 7.5-fold higher NIR absorbance than WS_2 UT.

Furthermore, TMDC produced by UT presented higher sizes than US samples. TMDC US revealed sizes of 548.2 ± 48.5 nm (MoS_2 US) and 340.0 ± 8.9 nm (WS_2 US). MoS_2 and WS_2 UT showed sizes of 724.3 ± 92.7 nm and 632.2 ± 8.9 nm, respectively. Samples produced by US also showed to have more negative surface charges than UT samples, revealing better water stability. Surface charges of MoS_2 and WS_2 US were –25.60 ± 1.81 and –33.30 ± 0.15 mV, respectively. UT samples revealed surfaces charges of –7.53 ± 0.287 (MoS_2 US) and –18.70 ± 0.52 mV (WS_2 US). MoS_2 US revealed a higher PDI (0.705 ± 0.053), compared with MoS_2 UT (0.612 ± 0.161). The same tendency was verified for WS_2 samples. WS_2 US showed a PDI of 0.456 ± 0.098, while WS_2 UT PDI was 0.431 ± 0.054.

Conclusions: The use of ultrasonication in the production of MoS_2 and WS_2 by PVP-assisted liquid phase exfoliation allowed to obtain materials with more efficient in converting NIR light into heat, with small sizes and lower surface charges, comparing with high shear mixing. MoS_2 US and UT and WS_2 US revealed their potential to act as mild-PTT agents, once all of them reached temperature above 45 °C.

References:

[1] Anju, S. and P. Mohanan, 271(2021).
[2] Costa-Almeida, R., *et al.*, 12(2020) 1840.
[3] Biccai, S., *et al.*, 6(2018).
[4] Paton, K.R., *et al.*, 13(2014) 624-630.

Acknowledgements:

This work was financially supported by LA/P/0045/2020 (ALiCE), UIDB/00511/2020 and UIDP/00511/2020 (LEPABE), UIDB/QUI/00616/2020 (CQVR), funded by national funds through FCT/MCTES (PIDDAC), base UIDB/04293/2020 Funding of the Institute for Research and Innovation in Health—i3S. This work was financed by FEDER funds through the COMPETE 2020—Operational Programme for Competitiveness and Internationalization (POCI), Portugal 2020. This work is financially supported by national funds through the FCT/MCTES (PIDDAC), under the UT Austin PT Program, under the project UTAP-EXPL/NPN/0044/2021 - 2D-Therapy, also under the FCT project 2022.04494.PTDC - PhotoRect. Project 2SMART—engineered Smart materials for Smart citizens, with reference NORTE-01-0145-FEDER-000054, supported by Norte Portugal Regional Operational Programme (NORTE 2020), under the PORTUGAL 2020 Partnership Agreement, through the European Regional Development Fund (ERDF). Artur Pinto thanks the Portuguese Foundation for Science and Technology (FCT) for the financial support of his work contract through the Scientific Employment Stimulus—Individual Call—(CEECIND/03908/2017). Filipa Silva (2021.05897.BD) and Bruno Freitas (2022.10443.BD) would like to thank FCT and European Social Fund (ESF) for financial support. Hui-Ping Chang would like to acknowledge the financial support from the UT-Portugal project (UTAP-EXPL/NPN/0044/2021) and the Ministry of Education of Taiwan.

172Fast-forward on skin wound resolution with antimicrobial and pro-angiogenic peptides: is covalent conjugation to norbornene-chitosan nanoparticles worth it?

Pedro M. Alves[1,2,3,4], Diana R. Fonseca[1,2,3], Sílvia J. Bidarra[1,2], Ana Gomes[4], Cristina C. Barrias[1,2], Paula Gomes[4], M. Cristina L. Martins[1,2,5,*]

[1]i3s, Instituto de Investigação e Inovação em Saúde, Universidade do Porto, Rua Alfredo Allen, 208, 4200-135 Porto, Portugal

[2]INEB, Instituto de Engenharia Biomédica, Universidade do Porto, Rua Alfredo Allen, 208, 4200-135 Porto, Portugal

[3]Faculdade de Engenharia, Universidade do Porto, Rua Dr. Roberto Frias, 4200-465 Porto, Portugal

[4]LAQV-REQUIMTE, Departamento de Química e Bioquímica, Faculdade de Ciências, Universidade do Porto, Rua do Campo Alegre 687, 4169-007 Porto, Portugal

[5]ICBAS - Instituto de Ciências Biomédicas Abel Salazar, Universidade do Porto, Rua de Jorge Viterbo Ferreira, 4050-313 Porto, Portugal

*Correspondence: cmartins@ineb.up.pt

Author Keywords: Norbornene-chitosan, Nanoparticles, Antimicrobial Peptides, Pro-angiogenic Peptides, Infection, Angiogenesis, Skin Chronic Wounds, *Staphyloccoccus epidermidis*, Human Umbilical Vein Endothelial Cells

Introduction: Non-healing chronic wound affect approximately 40 million patients worldwide, represent a market of 25 billion dollars in the US and their prevalence is expected to increase, due to rising rates in diabetes and obesity.[1]

Chronic wounds are wounds that heal slowly - in a period of more than 12 weeks. When a skin wound is established, an orchestrated process of healing starts in order to close it and repair the damaged tissue. However, when the process is disrupted, the wound can get chronically arrested in a stage of persistent inflammation.[2,3] This makes it harder for epidermal and dermal cells to respond to reparative stimuli. Due to exposure of skin wounds to the external environment, it is common for bacteria and other microorganisms to invade the injury. If bacteria are able to establish a biofilm, their removal by the immune system becomes harder and the wound healing process is further impaired.[4] Application of topical antiseptics or systemic antibiotics is often employed, but can suffer from limited residence time and can even lead to the induction of antimicrobial resistance. Alternatively, antimicrobial peptides can fight bacteria with a decreased likelihood of inducing resistance.[5] However, due to the high enzymatic load at the wound site, antimicrobial peptides may be better protected from degradation if covalently conjugated onto biomaterials.[6] Therefore, building on our previous works with carbodiimide[7] and copper catalyzed cycloaddition[5,8] chemistries, we herein used the highly efficient photo-initiated thiol-ene chemistry to conjugate an antimicrobial peptide, Dhvar-5 (LLLFLLKKRKKRKY-spacer-C), onto norbornene-modified chitosan nanoparticles (NorChit NPs). Thiol-ene reactions are triggered by UV (or other stimuli, such as heat) and occur between alkene and thiol-containing moieties, in the presence of a photoinitiator. Thiol-ene reactions occur with the use of any non-sterically hindered terminal ene, but reaction rates are faster when using electron-rich and/or strained enes, such as norbornenes.[9]

Furthermore, as chronic wounds are unable to progress into the proliferative stage, where angiogenesis would be stimulated by the secretion of growth factors - namely vascular endothelial growth factor (VEGF), the sprouting of blood vessels that would bring oxygen, nutrients and allow metabolite exchange does not take place.[10] Therapies based on growth-factors have been described, namely by delivery and/or promotion of VEGF activity. However, growth factors are equally susceptible to be degraded by the intense enzymatic activity present at the chronic wound.[6] To overcome this, we also conjugated a VEGF-mimicking peptide, QK (C-spacer-KLTWQELYQLKYKGI), to the NorChit NPs by thiol-ene chemistry.

Methodology: NorChit was synthesized as previously described by us.[11] NP production and peptide conjugation occurred in a microfluidics device coupled with UV LED (λ=365 nm). The microfluidics device had 3 inlets and 1 outlet to allow perfusion of NorChit, deionized water and peptide solutions containing the photoinitiator VA-086 through the device. Resulting NP were washed in 50-kDa Amicon® filter units. Peptide was quantified both in the supernatant and in the NP. Dhvar5-NorChit NP were tested on *Staphylococcus epidermidis* (ATCC 35984) for 6h in 50% Mueller-Hinton broth / 50% Phosphate Buffer Saline and also in 50% Mueller-Hinton broth / 50% Simulated Wound Fluid, in dynamic conditions. Moreover, a 3-day proliferation

assay using Human Umbilical Vein Endothelial Cells (HUVEC) was performed to test the pro-angiogenic potential of QK-NorChit NP when compared to bare NorChit NP and soluble VEGF and soluble QK peptide.

Results and discussion: Produced NP had an average diameter of 150 - 180 nm and were collected at 10^9 NP/mL. Nanoparticles with conjugated peptides had 40% (30 µg/mL) and 70% (70 µg/mL) of initial Dhvar5 and QK, respectively. Dhvar5-NorChit NP (10^8 NPs/mL) showed bactericidal effect, but even bare NorChit NP were able to cause a 1-log reduction in culturable bacteria, suggesting that free norbornene groups also have antimicrobial activity. Regarding proliferation, both bare and NorChit-QK NPs doubled the metabolic activity of HUVEC compared to control, while free QK peptide did not induce such increase, hinting that conjugation favors peptide activity. Once more, free norbornene groups appear to have bioactivity by stimulating metabolic activity of endothelial cells.

Conclusion: These results show that NorChit NP can tackle two hallmarks of chronic wounds - bacterial infection and impairment of endothelial cell proliferation. Their activity can be potentiated by the covalent conjugation of bioactive peptides. Therefore, terapies that combine nanoparticles decorated with antimicrobial and pro-angiogenic peptides may be used in the future to accelerate healing in skin chronic wounds.

References:

1. Sen, C. K. *et al.* Human skin wounds: A major and snowballing threat to public health and the economy. *Wound Repair and Regeneration* vol. 17 763–771 (2009).
2. Kim, H. S. *et al.* Advanced drug delivery systems and artificial skin grafts for skin wound healing. *Adv. Drug Deliv. Rev.* **146**, 209–239 (2019).
3. Demidova-Rice, T. N., Hamblin, M. R. & Herman, I. M. Acute and Impaired Wound Healing. *Adv. Skin Wound Care* **25**, 304–314 (2012).
4. Thapa, R. K., Diep, D. B. & Tønnesen, H. H. Topical antimicrobial peptide formulations for wound healing: Current developments and future prospects. *Acta Biomater.* **103**, 52–67 (2020).
5. Barbosa, M., Vale, N., Costa, F. M. T. A., Martins, M. C. L. & Gomes, P. Tethering antimicrobial peptides onto chitosan: Optimization of azide-alkyne "click" reaction conditions. *Carbohydr. Polym.* **165**, 384–393 (2017).
6. Alves, P. M., Barrias, C. C., Gomes, P. & Martins, M. C. L. Smart biomaterial-based systems for intrinsic stimuli-responsive chronic wound management. *Mater. Today Chem.* **22**, 100623 (2021).
7. Costa, F. ., Maia, S. R., Gomes, P. A. C. & Martins, M. C. L. Dhvar5 antimicrobial peptide (AMP) chemoselective covalent immobilization results on higher antiadherence effect than simple physical adsorption. *Biomaterials* **52**, 531–538 (2015).
8. Barbosa, M. *et al.* Antimicrobial coatings prepared from Dhvar-5-click-grafted chitosan powders. *Acta Biomater.* **84**, 242–256 (2019).
9. Hoyle, C. E. & Bowman, C. N. Thiol-ene click chemistry. *Angew. Chemie - Int. Ed.* **49**, 1540–1573 (2010).
10. Xue, M., Zhao, R., Lin, H. & Jackson, C. Delivery systems of current biologicals for the treatment of chronic cutaneous wounds and severe burns. *Adv. Drug Deliv. Rev.* **129**, 219–241 (2018).
11. Alves, P. M. *et al.* Thiol-Norbornene Photoclick Chemistry for Grafting Antimicrobial Peptides onto Chitosan to Create Antibacterial Biomaterials. *ACS Appl. Polym. Mater.* **4**, 5012–5026 (2022).

Acknowledgements:

FCT-MCTES through "Bio2SkinAdvanced" (NORTE-01-0247-FEDER-047225) and LAQV-REQUIMTE (UIDB/50006/2020). National (FCT/Norte 2020) and/or European Union funds (ESF – European Social Fund) support doctoral grants SFRH/BD/145471/2019 (PMA) and SFRH/BD/146890/2019 (DRF).

264*In vitro* characterization of different formulations of hydrogel-based dressings

Maria Gomes[1,2,3,*], Bruno Colaço[2], Pedro Gomes[3], Joana Barros[1]
[1]i3S – Instituto de Investigação e Inovação em Saúde, Universidade do Porto, Porto, Portugal
[2]Universidade de Trás-os-Montes e Alto Douro, Vila Real, Portugal
[3]Faculdade de Medicina Dentária, Universidade do Porto, Porto, Portugal
*Correspondence: mgomes@i3s.up.pt

Author Keywords: Biomaterials; Alginate; Collagen; Hyaluronic Acid; Biocompatibility; Tissue Regeneration

Introduction: While several approaches for wound healing are available, such as split- and full thickness skin grafts, as well as skin flaps, they are only moderately effective[1], which shows the need for more effective therapies for skin regeneration. The goal of tissue engineering and regenerative medicine is to create functional human tissue equivalents for organ repair, and to achieve this goal, engineered tissues must recreate the physical, chemical, and mechanical properties of "in vivo" tissues and replicate the complex interactions between cells and their microenvironments which regulate tissue morphogenesis, function, and regeneration[2].

In the last decades, bioactive dressings have been developed as innovative therapeutic approaches for the treatment of skin wounds, acting as biological matrices that promote healing[3,4]. Depending on their composition, they can promote different benefits in the treatment of wounds, namely, the creation of an adequate physiological environment – avoiding hypoxia, absorbing excess exudate, degrading necrotic tissues by enzymatic or autolytic action, and acting as a barrier against infectious agents[3,4].

Hydrogels are 3D cross-linked network systems composed of hydrophilic polymers that are important for tissue engineering due to their structural and compositional similarities to natural extracellular matrix (ECM). Due to the adjustable physical and chemical properties, hydrogels can also simulate the composition and mechanical properties of natural tissues, providing enough space and mechanical support for cell migration and tissue regeneration [5].

In addition to the aforementioned characteristics, dressings based on hydrogels of natural polymers, such as alginate, collagen and hyaluronic acid, have been used as transport systems for therapeutic agents due to the fact that they allow a sustained release of active substances at the injured site and present good pharmacokinetics, negligible side effects and a safe biodegrading profile[6]. Thus, this study aimed to characterize the physic-chemical properties and cytotoxicity of different hydrogel-based dressings formulations.

Methods: In this study, different formulations of the hydrogels-based alginate (Alg), collagen (Col), and hyaluronic acid (HA) were produced: Alg (control), Alg-Col and Alg-HA, using sol-gel and lyophilization methods.

The formulations were characterized according to their physic-chemical (attenuated total reflectance – Fourier transformed infrared spectroscopy (FTIR), scanning electron microscopy (SEM) and swelling tests) properties. Furthermore, it was assessed the cytotoxicity (metabolic activity assay) of hydrogels using L929 fibroblast cells.

Results: The ATR – FTIR spectra showed the characteristic peaks associated with Alg, Col and HA, indicating a successful entrapment of these elements into the alginate matrix without chemical reactions occurring between them. Through SEM analysis, it was shown that all hydrogels showed interconnected porous structures, with macro- and micro-pores formed alternately in the matrix. Alg and Alg-HA hydrogels showed a smooth surface, whereas Alg-Col hydrogels presented grooves and stretch marks well-embedded throughout the Alg matrix, as well as fibres across the pores, which was caused by the formation of collagen fibrils on the surface of the hydrogels. The swelling behaviour of the hydrogels was evaluated by measuring the changes in sample weight over time. For all samples, the swelling equilibrium was observed after 7 days, with the Alg-Col and Alg-HA hydrogels demonstrating a higher capacity for water absorption.

The L929 cultures' metabolic activity was evaluated by MTT assay and, both in the control conditions and in the presence of the hydrogels' extracts, the cells' metabolic activity increased throughout the culture period, with the Alg-Col hydrogel demonstrating a slightly higher activity than the other groups.

Conclusion: In conclusion, Alg-Col and Alg-HA hydrogels may be advantageous for wound healing due to their increased swelling ratio (the ability to adsorb the wound exudate) and water content (the ability to maintain a physiologically moist environment). It should be noted that none of the hydrogel formulations showed cytotoxicity, suggesting that they may be well suited for use in wound treatment.

References:

1. Fan F, Saha S, Hanjaya-Putra D. Biomimetic Hydrogels to Promote Wound Healing. *Front Bioeng Biotechnol*. 2021;9. doi:10.3389/fbioe.2021.718377

2. Sant S, Hancock MJ, Donnelly JP, Iyer D, Khademhosseini A. Biomimetic gradient hydrogels for tissue engineering. *Can J Chem Eng*. 2010;88(6):899- 911. doi:10.1002/cjce.20411

3. Shi C, Wang C, Liu H, et al. Selection of Appropriate Wound Dressing for Various Wounds. *Front Bioeng Biotechnol*. 2020;8:182. doi:10.3389/fbioe.2020.00182

4. Zhang X, Shu W, Yu Q, Qu W, Wang Y, Li R. Functional Biomaterials for Treatment of Chronic Wound. *Front Bioeng Biotechnol*. 2020;8:516. doi:10.3389/fbioe.2020.00516

5. Qi L, Zhang C, Wang B, Yin J, Yan S. Progress in Hydrogels for Skin Wound Repair. *Macromol Biosci*. 2022;22(7):2100475. doi:10.1002/mabi.202100475

6. Dhivya S, Padma VV, Santhini E. Wound dressings – a review. *Biomedicine (Taipei)*. 2015;5(4):22. doi:10.7603/s40681-015-0022-9

267A multifunctional gelatin-based gel for periodontal regeneration in dogs

Laura Pinho[1,2,3,4,5,*], André Queirós[6], Joana Marto[7], Catarina Santos[4,5], Bruno Colaço[2,3,8,9], Maria Helena Fernandes[1,2,*]

[1]BoneLab – Laboratory for Bone Metabolism and Regeneration, Faculdade de Medicina Dentária, Universidade do Porto, Rua Dr. Roberto Frias, 4200-465 Porto, Portugal

[2]LAQV/Requimte, Universidade do Porto, Rua Dr. Roberto Frias, 4200-465 Porto, Portugal

[3]CITAB - Centro de Investigação e de Tecnologias Agro-Ambientais e Biológicas, Universidade De Trás-os-Montes e Alto Douro, Quinta de Prados, 5000-801 Vila Real, Portugal

[4]EST - Escola Superior de Tecnologia, Instituto Politécnico de Setúbal, Estefanilha, 2910-761 Setúbal, Portugal

[5]CQE - Centro de Química Estrutural, Instituto Superior Técnico, Av. Rovisco Pais 1, 1049-001 Lisboa, Portugal

[6]SCIVET – Grupo Breed, R. Dr. José Bragança Tavares 78, 4580-593 Paredes, Portugal

[7]Research Institute for Medicines (iMed.ULisboa), Faculdade de Farmácia, Universidade de Lisboa, Avenida Professor Gama Pinto, 1649-003 Lisboa, Portugal

[8]AL4AnimalS - Laboratório Associado para a Ciência Animal e Veterinária, Universidade De Trás-os-Montes e Alto Douro, Quinta de Prados, 5000-801 Vila Real, Portugal

[9]CECAV - Centro de Ciência Animal e Veterinária, Universidade De Trás-os-Montes e Alto Douro, Quinta de Prados, 5000-801 Vila Real, Portugal

*Correspondence: laurapinho11@gmail.com and mhfernandes@fmd.up.pt

Author Keywords: Gelatin-based gels; multifunctional gels; periodontal regeneration; periodontal disease; dog

Introduction: Periodontal disease (PD) has a multifactorial etiology caused by plaque and an exacerbated inflammatory response and constitutes a serious problem both in dogs [1] and humans [2]. Disease development is divided into four sequential stages (gingivitis, mild, moderate, and severe periodontitis) being the later stage the most aggressive one [3, 4]. Late diagnosis of PD is responsible for the high prevalence of the disease in dogs [1, 5]. Due to poor oral hygiene, and oral cavity size, the evolution from gingivitis to severe periodontitis is quick and leads to the destruction of the periodontal tissue supporting the tooth (gingiva, periodontal ligament and alveolar bone) [5, 6]. The periodontal tissue is one of the most complex connective tissues due to the various cell types which interact to achieve the maintenance of all the tissues that compose the periodontium. The periodontal ligament plays a key role in protecting the oral cavity from microorganisms being fundamental to prevent the spread of PD [7-9]. Additionally, due to the complicated anatomy of the tooth and defect contours, there is an urgent need to develop solutions that can be customized, adjustable to the anatomy of the tooth, and allow the reconstruction of the lost function and the regeneration of periodontal tissue. To date, injectable hydrogels containing sodium alginate have been used as resorbable biomaterials for the treatment of PD due to their capacity for self-adaptation in variform periodontal defects [10]. However, in these systems, it is always necessary to wait for the gelation reaction. To avoid this waiting time, customizable 3D structures based on gelatin, hydroxyapatite (HA), graphene oxide (GO) and zinc oxide (ZnO) nanoparticles were developed in this work. The gelatin can act as a physical barrier to prevent cell invasion into the defect, is reabsorbable and simultaneously, can be useful in transporting nanoparticles with a leading role in the treatment of PD. Considering the relevance of maintaining the mechanical strength of bone, GO was added to the gelatin matrix.

Taking into account that bacteria are frequently detected in surgical periodontal procedures, ZnO nanoparticles were incorporated into the 3D gelatin structure due to their antibacterial properties. The bio-inspired HA nanoparticles were also added to promote rapid tissue regeneration.

The physicochemical properties and biological performance of the 3D gelatin-based hydrogels with GO/HA and GO/HA/ZnO were characterized in vitro to address canine periodontal regeneration.

Methodology: The composite gelatin-based hydrogels with GO (2 mg/mL), HA (20 mg/mL) and ZnO (25 mg/mL) nanoparticles were fabricated by a simple crosslinked hydrogel technique. The composite hydrogels

were kept at 75ºC for 1h in a water bath to promote an adequate crosslinking and homogenous composite hydrogel.

Periodontal ligament (PDL) derived cells were isolated from freshly extracted teeth from dog maxilla in a routine procedure. Periodontal ligament was cultured in basal medium (α-MEM, 10% fetal bovine serum and antibiotics) at 37°C in a 5% CO2 atmosphere until optimal cell density was achieved (~80% confluency). Subcultures 3rd to 5th passage were used in the experiments.

Sterilized 3D gelatin-based hydrogels with GO/HA or GO/HA/ZnO were incubated in basal medium for 6 hours (37°C, 5% CO2/air). After, PDL-derived cells were seeded on top of the hydrogels. At specific time points (1, 6, 12 and 20 days), seeded materials were characterized for cellular viability through the resazurin assay and imaging under scanning electron microscopy (SEM). SEM observation was performed using a High resolution (Schottky) Environmental Scanning Electron Microscope with X-Ray Microanalysis and Electron Backscattered Diffraction analysis: FEI Quanta 400 FEG ESEM / EDAX Genesis X4M. Cells cultured in the absence of the gels were used as control to confirm the suitability of the cell model. Comparison of the tested gels was assessed using the t-test and by the one-way analysis of variance (ANOVA), followed by the post hoc Tukey.

Results and Discussion: The structural integrity of the composite hydrogel is of key relevance for its functionality in the treatment of PD. It was observed that the addition of ZnO NPs to the composite hydrogel did not affect its structural integrity when compared to the hydrogel with GO/HA NPs. Additionally, it was observed that both 3D structures maintained their shape without collapse even after being cultured in a cell medium for 20 days. Conventional membranes often lack the necessary mechanical properties to repair periodontal tissue [11], but the developed organic-inorganic 3D structure seems to overcome this limitation.

Control cultures showed high viability/proliferation that increased with the incubation time. This behaviour suggested their suitability to address the performance of the two analyzed gels. Cellular viability in both GO/HA and GO/HA/ZnO composite hydrogels showed a significant increase throughout the days. Comparing both materials, cell viability was similar on day 1 but, afterwards, GO/HA/ZnO gel showed significantly higher values throughout the culture time (days 6, 12 and 20). SEM images confirmed this observation. These results translate into a proliferation of PDL-derived cells over time in both 3D gelatin-based hydrogels and strongly suggest a higher growth rate in the GO/HA/ZnO gel.

Conclusion: Composite hydrogels with structural integrity were developed by a simple crosslinked technique. The incorporation of GO, HA and ZnO NPs endowed the 3D structure with multifunctions. Moreover, the addition of ZnO NPs to the GO/HA hydrogel enhances the proliferation of dog PDL-derived cells without compromising the gel structural integrity, suggesting its potential for regenerative approaches in the management of tissue destruction in dog periodontal disease.

References:

1. Wallis, C. and L.J. Holcombe, A review of the frequency and impact of periodontal disease in dogs. Journal of Small Animal Practice, 2020. 61(9): p. 529-540.

2. Alawaji, Y.N., et al., Periodontal disease prevalence, extent, and risk associations in untreated individuals. Clin Exp Dent Res, 2022. 8(1): p. 380-394.

3. Fernandes, N., et al., Prevalence of periodontal disease in dogs and owners' level of awareness - a prospective clinical trial. Revista Ceres, 2012. 59: p. 446-451.

4. Niemiec, B.A., Periodontal Disease. Topics in Companion Animal Medicine, 2008. 23(2): p. 72-80.

5. Harvey, C.E., Management of periodontal disease: understanding the options. Vet Clin North Am Small Anim Pract, 2005. 35(4): p. 819-36, vi.

6. Matarese, G., et al., Implantology and Periodontal Disease: The Panacea to Problem Solving? Open Dent J, 2017. 11: p. 460-465.

7. Donos, N., et al., Description of the periodontal pocket in preclinical models: limitations and considerations. Periodontol 2000, 2018. 76(1): p. 16-34.

8. Yang, H., et al., Comparison of mesenchymal stem cells derived from gingival tissue and periodontal ligament in different incubation conditions. Biomaterials, 2013. 34(29): p. 7033-47.

9. Isaka, J., et al., Participation of periodontal ligament cells with regeneration of alveolar bone. J Periodontol, 2001. 72(3): p. 314-23.

10. Xu, Y., et al., Jelly-Inspired Injectable Guided Tissue Regeneration Strategy with Shape Auto-Matched and Dual-Light-Defined Antibacterial/Osteogenic Pattern Switch Properties. ACS Applied Materials & Interfaces, 2020. 12(49): p. 54497-54506.

11. Liu, X., et al., A biodegradable multifunctional nanofibrous membrane for periodontal tissue regeneration. Acta Biomater, 2020. 108: p. 207-222.

297Development of functionalized nanoparticles with an innovative microfluidics one-pot setup: proof of concept with chitosan and antimicrobial peptides for Helicobacter pylori management

Diana R. Fonseca[1,2,3], Pedro M. Alves[1,2,3], Estrela Neto[1,2], Beatriz Custódio[1,2,4], Sofia Guimarães[1,2], Marco Martins[5], Ana Gomes[7], Paula Gomes[7], Ruben Pereira[1,2,4], Paulo Freitas[5,6], Paula Parreira[1,2], M. Cristina L. Martins[1,2,4,*]

[1]i3S – Instituto de Investigação e Inovação em Saúde da Universidade do Porto, Porto, Portugal

[2]Instituto de Engenharia Biomédica, Universidade do Porto, Porto, Portugal

[3]Faculdade de Engenharia, Universidade do Porto, Porto, Portugal

[4]ICBAS—Instituto de Ciências Biomédicas Abel Salazar, Universidade do Porto, Porto, Portugal

[5]INL, International Iberian Nanotechnology Laboratory, Braga, Portugal

[6]INESC-MN, INESC Microsystems and Nanotechnologies, Lisboa, Portugal

[7]LAQV-REQUIMTE, Faculdade de Ciências, Universidade do Porto, Portugal

*Correspondence: cmartins@ineb.up.pt

Author Keywords: Biomaterials, gastric infection, covalent immobilization, norbornene-chitosan, surface modification

Extended Abstract: Antibiotic resistance is a main public health challenge, being described by the World Health Organization as one of the biggest threats to global health & development. The use of antimicrobial peptides (AMPs) is gaining relevance as an alternative to conventional antibiotics [1]. PexigananA (MSI-78A) is an analog of Pexiganan with reported bactericidal activity against Helicobacter pylori, a gastric bacterium that causes several gastric disorders and accounts for 90% of all diagnosed gastric cancers (5th most common & 4th deadliest worldwide) [2-4]. The immobilization of AMPs onto biomaterials overcomes their in vivo drawbacks since it avoids proteolytic degradation and aggregation with proteins. Plus, surface grafting of AMPs further enhances their bactericidal effect, as they become effective at lower concentrations than in solution [5].

Here, a versatile, cost-effective, and environmentally friendly “one-pot” microfluidics system suitable for nanoparticles (NPs) production and bioconjugation of any ligand containing a thiol group (e.g., cysteine amino acid) is proposed. In this innovative system, norbornene-modified chitosan nanoparticles were produced, and MSI-78A-SH was directly grafted on their surface (AMP-NP, 113 ± 2 nm), by Thiol–Norbornene “Photoclick” Chemistry. The reaction yield was ~40% (direct method- analysis of amino acids), and the grafting was confirmed by Fourier-transform infrared spectroscopy (FTIR), where the characteristic absorption bands of the AMP appeared at 1660 cm-1 (amide I) and 1530 cm-1 (amide II).

These AMP-NP maintained their integrity once exposed to acidic environment (pH 1.2), which validates the fitness of this approach for gastric applications.

The designed AMP-NP were tested against two highly pathogenic H. pylori strains (H. pylori 26695 and H. pylori J99) since multi-strain infection (in the same patient) is common, impairing the success of the therapy. Results demonstrate that AMP-NP (1011 NP/mL; 96 µg/mL AMP immobilized onto the surface) were bactericidal against both H. pylori strains, with full eradication of H. pylori 26695 in 30 min and of H. pylori J99 in 24h. The excellent bactericidal performance of AMP-NP against H. pylori 26695 may be linked with the AMP concentration, which is 3 times higher in NP than the minimum bactericidal concentration (MBC) of the free AMP (96 µg/mL versus 32 µg/mL [6]). Although H. pylori J99 strain eradication took 24h to reach, this strategy was advantageous for AMP performance, as the MBC of the free AMP was 128 µg/mL for this strain [6] and, when immobilized onto NP, lower amount of AMP (96 µg) was required. This effect may be associated with the high H. pylori –chitosan affinity that could further improve the killing effect. After exposure to AMP-NP, H. pylori membrane presented irregularities, the formation of vesicles and release of the intracellular content (transmission electron microscopy; TEM).

Furthermore, AMP-NP at the bactericidal concentration were cytocompatible against human gastric adenocarcinoma cell lines (AGS & MKN74, ATCC®), in accordance with ISO 10,993–5;12 [7,8].

Overall, a straightforward system to obtain AMP-conjugated chitosan nanoparticles was developed. Its main advantage is the possibility to simultaneously produce, crosslink and immobilize different thiolated-compounds onto the nanoparticles surface (due to Thiol–Norbornene "Photoclick" Chemistry), in the same device. This system was validated against the gastric pathogen, proving to be a step forward in the development of non-antibiotic approaches to counteract H. pylori infection and ultimately contribute to reduce the global gastric cancer burden. In the future, this microfluidic system can be further explored with other biomaterials and antimicrobial compounds for different applications.

References:

[1] A. Moretta et al., "Antimicrobial Peptides: A New Hope in Biomedical and Pharmaceutical Fields," Front Cell Infect Microbiol, vol. 11, Jun. 2021, doi: 10.3389/fcimb.2021.668632.

[2] P. Rawla and A. Barsouk, "Epidemiology of gastric cancer: Global trends, risk factors and prevention," Przeglad Gastroenterologiczny, vol. 14, no. 1. Termedia Publishing House Ltd., pp. 26–38, 2019. doi: 10.5114/pg.2018.80001.

[3] H. Sung et al., "Global cancer statistics 2020: GLOBOCAN estimates of incidence and mortality worldwide for 36 cancers in 185 countries," CA Cancer J Clin, Feb. 2021, doi: 10.3322/caac.21660.

[4] A. Neshani, H. Zare, M. R. Akbari Eidgahi, A. Hooshyar Chichaklu, A. Movaqar, and K. Ghazvini, "Review of antimicrobial peptides with anti-Helicobacter pylori activity," Helicobacter, vol. 24, no. 1. Blackwell Publishing Ltd, Feb. 01, 2019. doi: 10.1111/hel.12555.

[5] D. R. Fonseca et al., "Grafting MSI-78A onto chitosan microspheres enhances its antimicrobial activity," Acta Biomater, vol. 137, pp. 186–198, Jan. 2022, doi: 10.1016/J.ACTBIO.2021.09.063.

[6] P. Parreira et al., "Surface Grafted MSI-78A Antimicrobial Peptide has High Potential for Gastric Infection Management," Sci Rep, vol. 9, no. 1, Dec. 2019, doi: 10.1038/s41598-019-53918-4.

[7] Biological evaluation of medical devices, Part 12, Sample preparation and reference materials, SO 10993-12, 2004.

[8] Biological evaluation of medical devices Part 5, Tests for in vitro cytotoxicity, ISO 10993-5, 2009.

331MRI-based radiomics for assessment of the infrapatellar fat pad's influence on patellofemoral pain

Inês R. Campos[1,2,3,*], Rianne A. van der Heijden[3,4], Edwin H.G. Oei[3], Marienke van Middelkoop[5], Stefan Klein[3], Jaime S. Cardoso[1,6], Jukka Hirvasniemi[3]

[1]Faculdade de Engenharia, Universidade do Porto, Rua Dr. Roberto Frias, 4200-465 Porto, Portugal

[2]Instituto de Ciências Biomédicas Abel Salazar, Universidade do Porto, Rua Jorge de Viterbo Ferreira 228, 4050-313 Porto, Portugal

[3]Department of Radiology & Nuclear Medicine, Erasmus MC University Medical Center, P.O. Box 2040, 3000 CA Rotterdam, The Netherlands

[4]Department of Radiology, University of Wisconsin-Madison, Madison, WI, USA

[5]Department of General Practice, Erasmus MC University Medical Center, Rotterdam, The Netherlands

[6]Instituto de Engenharia de Sistemas e Computadores, Tecnologia e Ciência (INESC TEC), Rua Dr. Roberto Frias, 4200-465 Porto, Portugal

*Correspondence: up201806778@fe.up.pt

Author Keywords: Osteoarthritis, Infrapatellar Fat Pad, Segmentation, Machine Learning, Radiomics.

Introduction: Osteoarthritis (OA) is one of the most common causes of chronic disability in the elderly, representing an increasingly worrisome public health issue. OA is a whole joint disease, characterized by structural changes in different tissues, such as bone and the overlying cartilage [1]. Despite having pain as the main symptom, the pathophysiology behind the disease is still poorly understood and OA remains challenging to treat [2]. The knee is the most common site of OA [3].

Magnetic resonance imaging (MRI) is considered the most comprehensive imaging modality for knee OA (KOA) assessment [3][4]. MRI is able to depict all anatomic structures in the joint, even in the earliest stages of the disease [5][6][7]. Recent studies suggest that non-cartilaginous tissue changes play an important role in the onset and progression of KOA [8][9].

The infrapatellar fat pad (IPFP) is a highly vascularized soft tissue structure anterior to the knee joint [10]. The IPFP has been proposed as a possible source of knee pain in patients suffering from either OA or its supposed precursor, patellofemoral pain (PFP) [11][12]. PFP is a common condition in active young individuals, comprising pain behind and around the kneecap [13]. Recent findings suggest that inflammation of IPFP within the knee may have a central role in OA pain, contributing to its initiation and progression [14][15]. Additionally, MRI signal alterations are reportedly common within the IPFP in patients with KOA [11][12].

Radiomic methods were recently introduced to assess tissue characteristics, by quantitatively extracting a wide range of image features, allowing their correlation with biological markers and clinical outcomes [16]. Bone shape and texture variables have been previously extracted from knee MRI images, proving that MRI-based bone texture correlates with the actual three-dimensional microstructure of subchondral bone [17][18]. Likewise, radiomic features extracted from the femoral and tibial subchondral bone are different in knees with OA, validating their potential as quantitative biomarkers for investigating OA-related microstructural changes [17][19]. Finally, it has been shown that MRI-based three-dimensional texture of the IPFP is associated with future development of KOA [20][21]. Nonetheless, radiomic methods have not yet been widely used for the assessment of KOA and even less PFP.

Deep learning-based methods are increasingly used to automatically segment knee structures [22]. nnU-Net ("no new" U-net) is a deep learning-based segmentation method that automatically configures itself, fitting a variety of biomedical imaging data [23]. It has shown good results on many segmentation problems, which suggests it could be used to automatically segment the IPFP region.

Therefore, this study aims to extract radiomic features from the IPFP, using automatically segmented regions of interest from knee MRI images, and assess the ability of these radiomic features to distinguish between patients with PFP and healthy controls. Methods:

This study used data from the TripleP study [24]. The data included 64 patients with PFP (54.7% female, with a mean (standard deviation (SD)) age of 23.4 (7.0) years and body mass index (BMI) of 23.6 (3.8) kg/m2) and 70 controls (58.6% female, with a mean age of 23.1 (5.9) years and BMI of 22.3 (3.0) kg/m2). One knee of each participant was scanned using a 3-T scanner (Discovery MR750, GE Healthcare). Sagittal 3D non-fat-saturated fast-spoiled gradient-echo (non-FS FSPGR) sequence (field of view of 150 millimeters, in-plane resolution of 0.29 x 0.29 millimeters, slice thickness of 0.5 mm, echo time and repetition time of 5.4 and 17 milliseconds, respectively, flip angle of 12 degrees, and 216 slices) was used in the analyses.

The IPFP region of the 134 knees was automatically segmented using nnU-Net with the 3D U-Net configuration. The network was trained with 5-fold cross-validation using 30 manually segmented knees. The IPFP was segmented according to Van der Heijden et al [25]. Medial and lateral borders of the patella bone were used as anatomical landmarks.

The radiomic features were extracted using the open-source Workflow for Optimal Radiomics Classification toolbox (v. 3.6.0) [26]. Features related to orientation (n = 3), histogram (n = 13), shape (n = 21), original phase (n = 39) and texture (n = 376) were extracted (n = 452).

Elastic Net, a regularized regression that combines the L1 and L2 penalties of Lasso and Ridge regression methods, was used for dimensionality reduction and classification [27]. To compute it, the Stochastic Gradient Descent Classifier (SGDClassifier), an algorithm available in the Scikit-learn Python module, was selected [28]. The mixing parameter and regularization strength were optimized using 5-fold stratified cross-validation with a grid search and 10 repetitions. Three different models were evaluated: 1) basic model consisting of the demographic and anthropometric information of the patients (age, sex and BMI), 2) radiomic features model (n = 452), and 3) combination of models 1 and 2. The models' performances in distinguishing between subjects with and without PFP were evaluated using the area under the receiver operating characteristic and precision-recall curves (ROC AUC and PR AUC, respectively).

Results: The mean Dice similarity coefficient for the IPFP automatic segmentation was 0.94 (SD: 0.02). Visual evaluation of the automatically segmented IPFP showed that up to 15 slices of the most medial and lateral slices were not correctly segmented. To test the effect of the incorrectly segmented slices on the classification, 15 slices per side were removed from each segmentation mask, resulting in a set of "adjusted" masks. The radiomic features were extracted from both the original and adjusted masks.

The basic model had the highest ROC AUC for distinguishing between patients with and without PFP (ROC AUC of 0.69 (SD: 0.07) and PR AUC of 0.67 (SD: 0.15)). Regarding the features computed from the adjusted masks, analogous results were obtained for model 2 (ROC AUC of 0.58 (SD: 0.03) and PR AUC of 0.73 (SD: 0.03)) and model 3 (ROC AUC of 0.58 (SD: 0.02) and PR AUC of 0.74 (SD: 0.01)). Similar results were obtained using the features extracted from the original segmentation masks.

Texture features were split into subgroups to test the effect of texture feature type on the classification. Gabor filter features extracted from the adjusted masks resulted in a ROC AUC of 0.68 (0.04) and a PR AUC of 0.67 (0.10), whereas when combined with the basic model, the obtained ROC AUC was 0.69 (0.05) and PR AUC was 0.69 (0.07).

Discussion: The automatic segmentation of the IPFP using nnU-Net resulted in accurate segmentation masks, although some of the most medial and lateral slices were not correctly segmented. This could be related to the criteria of the manual segmentation used in the training data. Medial and lateral borders of the patella bone were used as starting and ending points of manual segmentation, even though the IPFP is present medially and laterally after these landmarks, making it difficult for nnU-Net to account for this. Nonetheless, visual evaluation confirmed the accurate segmentation of the central slices with visible patella bone. One study by Yu et al. automatically segmented the IPFP using 2.5D U-Net, resulting in a slightly lower Dice coefficient (0.90) than the one obtained in the current study [21]. This denotes the potential of nnU-Net (3D U-Net configuration) to automatically segment biomedical structures and proves its suitability for this task in particular.

Regarding the classification based on Elastic Net, texture features, such as Gabor filter, Gray-Level Co-Occurrence Matrix (GLCM), GLCM Multi Slice (GCLMMS) and Grey-Level Run Length Matrix (GLRLM) resulted in a ROC AUC above 0.60. In majority of the texture feature subgroups, the ROC AUC values improved when combining the features with the patients' information. Overall, the results show that some radiomic features from the IPFP differ between knees with and without PFP. In particular, the results suggest that Gabor filter, GCLM, GCLMMS and GLRLM texture features are promising quantitative imaging biomarkers. Our results are

in line with previous studies that have shown that IPFP radiomic features, especially texture-related, are relevant predictors of OA [20][21]. To our knowledge, no studies have analyzed the correlation between radiomic features and PFP. Future improvements could include exploring different post-processing algorithms for slice correction or exclusion and analysing other knee structures (such as bone). Furthermore, it might be interesting to apply these methods to other datasets, based on different MRI sequences, and test the classification using models that include different radiomic features' combinations.

Conclusion: In conclusion, nnU-Net proved to be applicable for the automatic segmentation of the IPFP in sagittal 3D non-FS FSPGR knee MRI images. Additionally, the results demonstrated that some texture features, such as Gabor filter, GCLM, GCLMMS and GLRLM features, are promising quantitative imaging biomarkers for the assessment of PFP.

References:

[1] Cross, M., Smith, E., Hoy, D., Nolte, S., Ackerman, I., Fransen, M., . . . March, L. (2014, July 19). The global burden of hip and knee osteoarthritis: Estimates from the global burden of disease 2010 study. Annals of the Rheumatic Diseases, 73(7), 1323-1330. doi:10.1136/annrheumdis-2013-204763.

[2] Primorac, D., Molnar, V., Rod, E., Jeleč, Ž, Čukelj, F., Matišić, V., . . . Borić, I. (2020). Knee osteoarthritis: A review of pathogenesis and state-of-the-art non-operative therapeutic considerations. Genes, 11(8), 854. doi:10.3390/genes11080854

[3] Hunter, D. J., & Bierma-Zeinstra, S. (2019). Osteoarthritis. The Lancet, 393(10182), 1745-1759. doi:10.1016/s0140-6736(19)30417-9

[4] Lespasio, M. J., Piuzzi, N. S., Husni, M. E., Muschler, G. F., Guarino, A., & Mont, M. A. (2017). Knee osteoarthritis: A Primer. The Permanente Journal, 21(4). doi:10.7812/tpp/16-183 [5] Roemer, F., Guermazi, A., Demehri, S., Wirth, W., & Kijowski, R. (2022). Imaging in osteoarthritis. Osteoarthritis and Cartilage, 30(7), 913-934. doi:10.1016/j.joca.2021.04.018

[6] Guermazi, A., Niu, J., Hayashi, D., Roemer, F. W., Englund, M., Neogi, T., . . . Felson, D. T. (2012). Prevalence of abnormalities in knees detected by MRI in adults without knee osteoarthritis: Population based observational study (Framingham osteoarthritis study). BMJ, 345(Aug29 1). doi:10.1136/bmj.e5339

[7] Hayashi, D., Felson, D., Niu, J., Hunter, D., Roemer, F., Aliabadi, P., & Guermazi, A. (2014). Pre-radiographic osteoarthritic changes are highly prevalent in the medial patella and medial posterior femur in older persons: Framingham OA Study. Osteoarthritis and Cartilage, 22(1), 76-83. doi:10.1016/j.joca.2013.10.007

[8] Roemer, F. W., Felson, D. T., Wang, K., Crema, M. D., Neogi, T., Zhang, Y., . . . Guermazi, A. (2012). Co-localisation of non-cartilaginous articular pathology increases risk of cartilage loss in the tibiofemoral joint—the most study. Annals of the Rheumatic Diseases, 72(6), 942-948. doi:10.1136/annrheumdis-2012-201810

[9] Guermazi, A., Roemer, F., Crema, M., Englund, M., & Hayashi, D. (2014). Imaging of non-osteochondral tissues in osteoarthritis. Osteoarthritis and Cartilage, 22(10), 1590-1605. doi:10.1016/j.joca.2014.05.001

[10] Stephen, J. M., Sopher, R., Tullie, S., Amis, A. A., Ball, S., & Williams, A. (2018). The infrapatellar fat pad is a dynamic and mobile structure, which deforms during knee motion, and has proximal extensions which wrap around the patella. Knee Surgery, Sports Traumatology, Arthroscopy, 26(11), 3515-3524. doi:10.1007/s00167-018-4943-1

[11] Ioan-Facsinay, A., & Kloppenburg, M. (2013). An emerging player in knee osteoarthritis: The infrapatellar fat pad. Arthritis Research & Therapy, 15(6), 225. doi:10.1186/ar4422 [12] De Vries, B. A., Van der Heijden, R. A., Poot, D. H., Van Middelkoop, M., Meuffels, D. E., Krestin, G. P., & Oei, E. H. (2020). Quantitative DCE-MRI demonstrates increased blood perfusion in Hoffa's fat pad signal abnormalities in knee osteoarthritis, but not in patellofemoral pain. European Radiology, 30(6), 3401-3408. doi:10.1007/s00330-020-06671-6

[13] Van der Heijden, R. A., Lankhorst, N. E., Van Linschoten, R., Bierma-Zeinstra, S. M., & Van Middelkoop, M. (2015). Exercise for treating patellofemoral pain syndrome. Cochrane Database of Systematic Reviews. doi:10.1002/14651858.cd010387.pub2

[14] Belluzzi, E., Stocco, E., Pozzuoli, A., Granzotto, M., Porzionato, A., Vettor, R., . . . Macchi, V. (2019). Contribution of infrapatellar fat pad and synovial membrane to knee osteoarthritis pain. BioMed Research International, 2019, 1-18. doi:10.1155/2019/6390182 [15] Inomata, K., Tsuji, K., Onuma, H., Hoshino, T., Udo, M., Akiyama, M., . . . Koga, H. (2019). Time course analyses of structural changes in the infrapatellar fat pad

and synovial membrane during inflammation-induced persistent pain development in rat knee joint. BMC Musculoskeletal Disorders, 20(1). doi:10.1186/s12891-018-2391-1

[16] Kumar, V., Gu, Y., Basu, S., Berglund, A., Eschrich, S. A., Schabath, M. B., . . . Gillies, R. J. (2012). Radiomics: The process and the challenges. Magnetic Resonance Imaging, 30(9), 1234-1248. doi:10.1016/j.mri.2012.06.010

[17] Hirvasniemi, J., Klein, S., Bierma-Zeinstra, S., Vernooij, M. W., Schiphof, D., Oei, E. H. (2021). A machine learning approach to distinguish between knees without and with osteoarthritis using MRI-based radiomic features from tibial bone. European Radiology, 31(11), 8513-8521. doi:10.1007/s00330-021-07951-5

[18] MacKay, J. W., Kapoor, G., Driban, J. B., Lo, G. H., McAlindon, T. E., Toms, A. P., . . . Gilbert, F. J. (2018). Association of subchondral bone texture on magnetic resonance imaging with radiographic knee osteoarthritis progression: Data from the Osteoarthritis Initiative Bone Ancillary Study. European Radiology, 28(11), 4687-4695. doi:10.1007/s00330-018-5444-9

[19] Xue, Z., Wang, L., Sun, Q., Xu, J., Liu, Y., Ai, S., . . . Liu, C. (2022). Radiomics analysis using MR imaging of subchondral bone for identification of knee osteoarthritis. Journal of Orthopaedic Surgery and Research, 17(1). doi:10.1186/s13018-022-03314-y

[20] Li, J., Fu, S., Gong, Z., Zhu, Z., Zeng, D., Cao, P., . . . Ding, C. (2022). MRI-based texture analysis of infrapatellar fat pad to predict knee osteoarthritis incidence. Radiology, 304(3), 611-621. doi:10.1148/radiol.212009

[21] Yu, K., Ying, J., Zhao, T., Lei, L., Zhong, L., Hu, J., . . . Zhang, X. (2023). Prediction model for knee osteoarthritis using magnetic resonance–based radiomic features from the infrapatellar fat pad: Data from the osteoarthritis initiative. Quantitative Imaging in Medicine and Surgery, 13(1), 352-369. doi:10.21037/qims-22-368

[22] Oei, E., Hirvasniemi, J., Van Zadelhoff, T., & Van der Heijden, R. (2022). Osteoarthritis year in Review 2021: Imaging. Osteoarthritis and Cartilage, 30(2), 226-236. doi:10.1016/j.joca.2021.11.012

[23] Isensee, F., Jaeger, P. F., Kohl, S. A., Petersen, J., & Maier-Hein, K. H. (2020). NNU-net: A self-configuring method for deep learning-based biomedical image segmentation. Nature Methods, 18(2), 203-211. doi:10.1038/s41592-020-01008-z

[24] Van der Heijden, R. A., Oei, E. H., Bron, E. E., Van Tiel, J., Van Veldhoven, P. L., Klein, S., . . . Van Middelkoop, M. (2016). No difference on quantitative magnetic resonance imaging in patellofemoral cartilage composition between patients with patellofemoral pain and healthy controls. The American Journal of Sports Medicine, 44(5), 1172-1178. doi:10.1177/0363546516632507

[25] Van der Heijden, R. A., De Vries, B. A., Poot, D. H., Van Middelkoop, M., Bierma-Zeinstra, S. M., Krestin, G. P., & Oei, E. H. (2021). Quantitative volume and dynamic contrast-enhanced MRI derived perfusion of the infrapatellar fat pad in patellofemoral pain. Quantitative Imaging in Medicine and Surgery, 11(1), 133-142. doi:10.21037/qims-20-441

[26] Starmans, M., Klein, S., Van der Voort, S. R., Thomeer, M. G., Miclea, R. L., & Niessen, W. J. (2018). Classification of malignant and benign liver tumors using a radiomics approach. Medical Imaging 2018: Image Processing. doi:10.1117/12.2293609

[27] Zou, H., & Hastie, T. (2005). Regularization and variable selection via the elastic net. Journal of the Royal Statistical Society Series B: Statistical Methodology, 67(2), 301-320. doi:10.1111/j.1467-9868.2005.00503.x

[28] Pedregosa, F., Varoquaux, G., Gramfort, A., Michel, V., Thirion, B., Grisel, O., Blondel, M., Prettenhofer, P., Weiss, R., Dubourg, V., Vanderplas, J., Passos, A., Cournapeau, D., Brucher, M., Perrot, M. & Duchesnay, E. (2011). Scikit-learn: Machine Learning in Python. Journal of Machine Learning Research, 12, 2825-2830.

361Phase Analysis of Back-Scattering Signals from Optical Fiber Tweezers for Bioparticles Detection and Differentiation

Beatriz Barros, João Paulo Cunha*

Center for Biomedical Engineering Research, Institute for Systems and Computer Engineering, Technology and Science (INESCTEC) Rua Dr.Roberto Frias, 4200-465, Porto, Portugal

Faculdade de Engenharia, Universidade do Porto Rua Dr. Roberto Frias, 4200-465 Porto, Portugal

*Correspondence: jpcunha@fe.up.pt

Introduction: One of the most promising approaches to disease diagnosis and prognosis is the detection of biomarkers such as circulating tumor cells, RNA, proteins, extracellular vesicles (EVs), among others, in human circulating fluids (blood, serum, plasma). The measurement and evaluation of such molecules allows the detection of changes in composition and concentration that can be indicators of pathogenic processes or pharmacologic responses to therapeutic interventions [1].

Despite the major potential of biomarker-identification strategies, the detection of structures with such reduced size is a challenging task for conventional single-cell techniques, limited by their bulky systems and inherent diffraction barrier of light. Therefore, the development of selective, sensitive, and reliable analytical devices, capable of detecting and discriminating different classes of biological particles at low concentrations, and cope with the challenges associated with in-vivo measurements, is highly demanded by healthcare and pharmaceutical systems [2]. The vast majority of sensing/detection configurations are highly dependent of transduction labelling elements (fluorescent dyes or radioactive isotopes) to generate a physically readable signal or require sophisticated chemistry to enhance biochemical interactions in specific spatial locations, which introduces additional processes for attaching and removing the analyte, increasing the cost and complexity and reducing the detection speed . Besides, since the signal is usually generated through highly specific chemical functionalization processes and antigen-antibody interactions, it is only possible to measure a single attribute, while the sensor output signal can contain much more information that could be used to perform a more complete analysis. To tackle these challenges, we introduce a new paradigm for label-free single-particle bio detection based on exploring phase spectral information of back-scattering signals acquired from an optoelectronic Optical Fiber Tweezers (OFTs) setup, conceptualized and developed on our laboratory in previous works [3]–[5]. Through Optical Trapping phenomena, individual particles are immobilized at the tip of an optical fiber. We show that the signal returned by each trapped particle (back-scattering signal), due to light-matter interactions, contains patterns in the phase spectrum related to the inherent properties of the particle under analysis, that can be used to compute mathematical features able to detect and differentiate particles of different sources, size and complexity degree [6].

Methods: The visualization, manipulation and acquisition of the back-scattering signal occurs through an optical setup composed by an inverted microscope, a motorized micromanipulator holding an optical fiber tip, and a signal acquisition module. A stable trapping of particles is ensured by a polymeric spherical lens fabricated on top of the optical fiber. The back-scattering signals analyzed include two synthetic (Polystyrene, PMMA) and one simple biological (Living yeast cell) microparticles and two complex human cancer-derived cells, Mock and HST6 cancer cells (MKN45 gastric cell line), suspended in Phosphate Buffered Saline (PBS). These present the same genetic composition and morphology, only differing in the surface glycosylation since HST6 cells are transfected with a vector over-expressing an enzyme leading to the biosynthesis of the well-established tumor-derived carbohydrate STn antigen, associated with metastasis and poor prognosis of cancer patients [7]. After acquisition, each signal was analyzed and processed through a MATLAB 2019b® custom-built script for signal pre-processing and phase spectrum calculation, through the Fourier Transform. Phase-related information was then exploited through a subset of features based on descriptive statistics containing 7 measurements extracted from the phase spectrum, namely, Standard Deviation (STD), Root Mean Square (RMS), Interquartile (IQR), Range, Kurtosis, Variance and Entropy. A second subset of features was applied based on FFT coefficients. This was followed by a statistical analysis stage where each feature was individually evaluated between the selected classes for each problem, considering 4 class comparisons using Kruskal-Wallis test followed by 2-class comparisons through Mann-Whitney test, with a significance threshold of p-value=0.05 being considered for tests conducted.

Results: Both the statistical features and FFT phase coefficients present a statistically significant difference between the two synthetic particles (Polystyrene, PMMA) and yeast cell. In the experiment considering the two complex human cancer-derived cells, the phase-derived parameters showed to be suitable not only to identify the presence of a trapped particle but also to discriminate between biological (tumoral cells) vs synthetic (PS) particles and even between the two very similar biological (cancer) cells (Mock and HST6), with statistical significance. A higher discrimination power is observed for more complex biological particles, which indicates that the computed features are robust to deal with the heterogeneity and complexity degree of biological particles and environment.

Conclusion: We explored the potential of phase spectral information for detection and discrimination of micro (bio)particles present in different liquid suspensions used in biological assays. The results reveal that phase is a potential new contributor to obtain discriminative light patterns strongly related to the structural properties of each cell, that are enhanced with an increase in particle complexity and heterogeneity degree. The presented subset of features was capable of successfully discriminate two highly similar human cancer cells, only differing in the surface glycosylation patterns. This is an extraordinary outcome in view of the current challenges of cancer and other diseases detection methodologies based on singlecell fast screening and, specifically, using optical fiber for signal detection. Since these are slight cellular changes, only rather expensive affinity, and biochemical assays, involving fluorescence, or highly sensitive spectral and imaging techniques are able to detect them. In this context, the sensitivity of the phase-based features to cancer-associated glycoforms expressed at the surface presents a great potential for single-cell characterization methods such as low-cost cancer biomarker assays. Considering the growing importance of nanotechnologies, we intend to follow our study from micro to nano-sized particles and experiment our phase-based approach for detection and discrimination of nano-sized particles (e.g. exosomes) suspended in biofluids (e.g. blood plasma) in order to assess the discriminative potential of phase for smaller target dimension bioparticles. One major advantage of this approach is the possibility to be adapted and scaled to research environments and challenges of different scientific areas. The heterogeneity found at the single-cell level is crucial for accurate diagnostic and therapeutic results of diseases, but it is largely masked by the analysis of average responses from a population. To comprehensively understand cell heterogeneity, manipulation, and analysis of cells at the single-cell level is highly demanded, in a large variety of scenarios. For instance, in Neuroscience research, access the individual cell types in in a given neural circuit is crucial to reveal the mechanisms behind the organization and operation of brain activity, composed by a vast diversity in cell types, subtypes, and states [8].

We postulate that the presented approach can evolve to a highly versatile platform for in-vivo, label free manipulation, detection and identification capabilities to be deployed on multifunctional single-molecule analytic tools applicable in a wide variety of scientific fields.

References:

[1] B. J. Battersby, A. Chen, D. Kozak, and M. Trau, “7 - Biosensors for disease biomarker detection,” in Biosensors for Medical Applications, S. Higson, Ed., in Woodhead Publishing Series in Biomaterials. Woodhead Publishing, 2012, pp. 191– 216. doi: 10.1533/9780857097187.2.191.

[2] S. Tabassum and R. Kumar, “Advances in Fiber-Optic Technology for Point-of-Care Diagnosis and In Vivo Biosensing,” Adv. Mater. Technol., vol. 5, no. 5, p. 1900792, 2020, doi: 10.1002/admt.201900792.

[3] J. S. Paiva et al., “iLoF: An intelligent Lab on Fiber Approach for Human Cancer Single-Cell Type Identification,” Sci. Rep., vol. 10, no. 1, Art. no. 1, Feb. 2020, doi: 10.1038/s41598-020-59661-5.

[4] J. S. Paiva, R. S. R. Ribeiro, J. P. S. Cunha, C. C. Rosa, and P. A. S. Jorge, “Single Particle Differentiation through 2D Optical Fiber Trapping and Back-Scattered Signal Statistical Analysis: An Exploratory Approach,” Sensors, vol. 18, no. 3, Art. no. 3, Mar. 2018, doi: 10.3390/s18030710.

[5] J. S. Paiva, P. S. Jorge, and J. P. S. Cunha, “DEVICE AND METHOD FOR DETECTING AND IDENTIFYING EXTRACELLULAR VESICLES IN A LIQUID DISPERSION SAMPLE,” 2020

[6] B. J. Barros and J. P. S. Cunha, “Micron-Sized Bioparticles Detection through Phase Analysis of Back-Scattering Signals from Optical Fiber Tweezers: An Exploratory Study,” in 2022 IEEE 21st Mediterranean Electrotechnical Conference (MELECON), Jun. 2022, pp. 271–275. doi: 10.1109/MELECON53508.2022.9843085.

[7] N. T. Marcos et al., “Role of the human ST6GalNAc-I and ST6GalNAc-II in the synthesis of the cancer-associated Sialyl-Tn antigen,” Cancer Res., vol. 64, no. 19, pp. 7050–7057, 2004, doi: 10.1158/0008-5472.CAN-04-1921.

[8] H. Zeng and J. R. Sanes, “Neuronal cell-type classification: challenges, opportunities and the path forward,” Nat. Rev. Neurosci., vol. 18, no. 9, Art. no. 9, Sep. 2017, doi: 10.1038/nrn.2017.85.

376Functionalization with cannabidiol increases the BBB targeting capacity of small-sized lipid nanocapsules

Alexandre Pérez-López[1,*], Juan Aparicio-Blanco[1], Cristina Martín-Sabroso[1], Juan F González-Matilla[2], Ana I Torres Suárez[1]

[1]Department of Pharmaceutics and Food Technology, Faculty of Pharmacy, Complutense University., Av. Séneca, 2, 28040 Madrid, Spain

[2]Department of Chemistry in Pharmaceutical Sciences, Faculty of Pharmacy, Complutense University., Av. Séneca, 2, 28040 Madrid, Spain

*Correspondence: alexap03@ucm.es

Author Keywords: Cannabinoids, lipid nanocapsules, blood brain barrier, brain targeting.

Introduction: Central Nervous System (CNS) diseases remain one of the greatest health-care challenges of the 21st century. This is mainly due to the difficulty of most current treatments to bypass the Blood Brain Barrier (BBB). In this context, the active vectorization of small-sized lipid nanocapsules (LNCs) with Cannabidiol (CBD) arises as an appealing strategy to selectively target the BBB [1]. For this purpose, CBD was covalently incorporated at the surface of 20 nm sized LNCs. Then, in vitro experiments were performed in order to assess the capacity of the LNCs to selectively target and cross the BBB.

Materials and methods:

Materials

Kolliphor HS15, Labrafac WL 1349, Lipoid® S75, MilliQ water, NaCl, mono-alkylated CBD and 3,3'-dioctadecyloxacarbocyanine perchlorate (DiO) were used to prepare the LNCs. Endothelial basal medium-2 (EBM-2), Dulbecco's modified Eagle's medium (DMEM), tetramethylrhodamine isothiocyanate (TRITC)–Dextran (150 KDa), type I collagen from calf skin, fibronectin from bovine plasma and ThinCert® cell culture inserts (pore size: 1.0 µm; area: 1.1 cm2) for the in vitro experiments.

Preparation and characterization of LNCs

LNCs were prepared by the phase inversion temperature technique [2]. For the preparation of CBD-LNCs, azyde-Kolliphor HS15 was used. Then, the obtained azided-LNCs were covalently functionalized with mono-alkylated CBD using "click chemistry". For tracking purposes, the fluorescent dye DiO was dissolved in the oily core of the LNCs. All formulations were quantitatively characterized in terms of volume diameter and polydispersity index (PdI). Additionally, the functionalization rate of CBD-LNCs was qualitatively and quantitatively characterized with Nuclear Magnetic Resonance and UV-spectroscopy, respectively.

In vitro cellular uptake

To quantitatively evaluate the BBB-targeting ability of LNCs, the hCMEC/D3 cell line was seeded into collagen-coated 12-well plates. After 72 h, medium was replaced by DiO-labelled LNCs (3 µg DiO/ mL) and cells were further incubated for 24 h. The fluorescence intensity of cells was analyzed by flow cytometry (CytoFLEX, Beckman Coulter; λ excitation: 488 nm; λ emission: 530 nm).

Transport of the LNCs across an in vitro 2D BBB model

Assembling the model and evaluation of the monolayer integrity

An in vitro BBB healthy 2D model consisting of a monolayer of hCMEC/D3 cells was established. Succinctly, cells were seeded into collagen- and fibronectin-coated 12-well cell culture inserts at confluence and incubated for 72 h. Before evaluating the transport across the model, the monolayer integrity was assessed by determining the permeability coefficient of the hydrophilic tracer TRITC-Dextran at 24h both in the presence and the absence of LNCs [3]. The concentration of TRITC-dextran was determined using a microplate reader (Varioskan Flash, ThermoFisher; λ excitation: 544 nm, λ emission: 590 nm). Furthermore, the Trans-Endothelial Electrical Resistance (TEER) across the model was also measured with a Volth/Ohm meter (Millicell ERS-2, Merck).

Transport across the monolayer of brain endothelial cells

The BBB transcytosis ability of the LNCs was evaluated. Succinctly, 400 µL of a suspension of DiO-labeled LNCs (3 µg DiO/ mL) was added to the apical chamber of both cell-seeded and non-seeded inserts. The concentration of DiO at 24 h was determined using a microplate reader (λ excitation: 485 nm, λ emission: 520 nm) and used to calculate the permeability coefficients [3].

Results and discussion:

Preparation and characterization of LNCs

LNCs of 20 nm without CBD (F1) and functionalized with CBD (F2) were obtained. The functionalization resulted in a statistically significant increase in their volume diameter, compared with the non-functionalized LNCs, probably due to the incorporation of CBD at the surface (Figure 1). However, the functionalization process did not alter the dispersity of the LNCs.

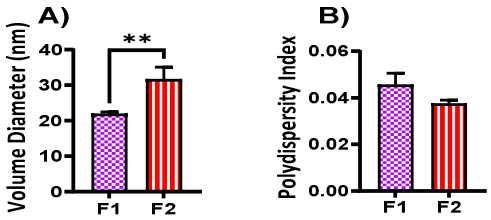

Figure 1. Comparative in terms of A) volume diameter and B) PdI of blank LNCs before and after incorporation of CBD. ** ($p<0.01$). n=3. Student t test. Mean ± SD.

In vitro cellular uptake

The internalization of fluorescent CBD-LNCs by the brain endothelial cell line was significantly increased by 150.9 % compared with the non-functionalized LNCs (Figure 2A). Hence, the decoration with CBD increased the BBB targeting ability of the formulations.

Transport of the LNCs across an in vitro 2D BBB model

Assembling the model and evaluation of the monolayer integrity

As shown in Figure 2B and C, the permeability of TRITC-Dextran and the TEER values across the monolayer of endothelial cells were similar in the presence and absence of non- and CBD-LNCs. Therefore, the functionalization process of LNCs did not alter the BBB barrier properties.

Transport across the monolayer of brain endothelial cells

Regarding the effect of the decoration with CBD on the transport across the model, no significant differences were observed between the permeability coefficients at 24 hours (Figure 2D). However, 2D models to date have failed to fully reproduce the human anatomical complexity of the BBB, so that these permeability values might be inaccurate estimated as the receptors by CBD triggers transcytosis in endothelial cells may not be expressed in this 2D BBB model [4].

Conclusions: The functionalization process significantly increased the size of highly monodisperse LNCs. Furthermore, although the incorporation of CBD showed no effect on the permeability coefficients, it significantly enhanced the BBB-targeting ability of the LNCs. In the future, more permeability studies must be performed in BBB models with more physiological relevance (3D) to ensure the potential of CBD to efficiently increase the passage across the brain endothelium of CNS nanomedicines.

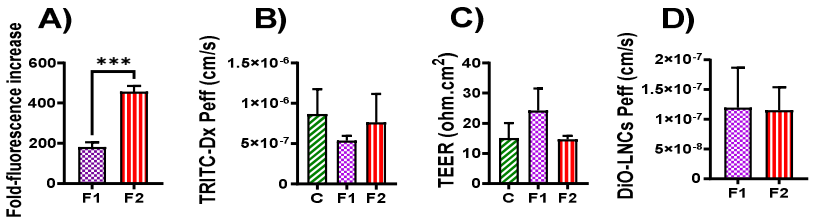

Figure 2. A) Quantitative evaluation of the in vitro cellular uptake into the hCMEC/D3 cell line at 24h of DiO loaded non-CBD functionalized (F1) and CBD functionalized (F2) LNCs by flow cytometry expressed as folds increase in mean fluorescence intensity vs control (non-treatment). n=3. Student t test. *** ($p<0.001$) respect to the control. B) TRITC-dextran effective permeability coefficients and C) trans-endothelial electrical resistance (TEER) across the hCMEC/D3 cell monolayer at 24 h in absence and presence of blank non and CBD functionalized LNCs. n=3-12. One way ANOVA. D) In vitro permeability coefficients at 24 h of DiO loaded non- and CBD functionalized LNCs. n=5. Student t test. Data are expressed as mean +/- SD.

References:

[1] Pisanti, S et al., Pharmacol. Ther. 175, 133-175 (2017).

[2] Aparicio-Blanco, J et al. J Biomed Nanotechnol. 15, 1149 (2019).

[3] Aparicio-Blanco, J et al. Mol. Pharm. 16(5):1999–2010 (2019).

[4] Pérez-López, A et al. Adv. Drug Deliv. Rev. 196, 114816 (2023).

Acknowledgements:

This work was funded by the Spanish Ministry of Science, Innovation and Universities research project PID2019-105531RB-I00/ AEI / 10.13039/501100011033.

378Poly(lactic-co-glycolic acid)/graphene nanoparticles for combined drug delivery and cancer phototherapy

Bruno Freitas[1,2,3,*], Filipa A. L. S. Silva[1,2,4], José Ramiro Fernandes[5,6], Susana G. Santos[2,4], Maria J. Oliveira[2,4], Joana Paredes[2,3,7], Fernão D. Magalhães[1], Artur M. Pinto[1,2,4,*]

[1]LEPABE - Laboratory for Process Engineering, Environment, Biotechnology and Energy, Faculdade de Engenharia, Universidade do Porto, 4200-180 Porto, Portugal

[2]i3S - Instituto de Investigação e Inovação em Saúde, Universidade do Porto, Rua Alfredo Allen, 208, 4200-180 Porto, Portugal

[3]IPATIMUP - Instituto de Patologia e Imunologia Molecular da Universidade do Porto, Universidade do Porto, 4200-180 Porto, Portugal

[4]INEB - Instituto de Engenharia Biomédica, Universidade do Porto, Rua Alfredo Allen, 208, 4200-180 Porto, Portugal

[5]CQVR – Centro de Química Vila Real, Universidade de Trás-os-Montes e Alto Douro, Portugal

[6]Physical Department, University of Trás-os-Montes and Alto Douro, Vila Real, Portugal

[7]Faculty of Medicine, University of Porto, 4200-319 Porto, Portugal

*Correspondence: bfreitas@i3s.up.pt and arturp@fe.up.pt

Author Keywords: Hybrid nanocarrier, 2D material, Phototherapy, Cancer, Controlled release

Extended Abstract: Cancer is a multifaceted disease that requires a complex array of treatments. Millions of patients are affected worldwide and many more close family members and friends are affected by treatment-related consequences. This disease is one of the leading causes of death worldwide, even more as the global population ages. Factors like lifestyle and exposure to potentially carcinogenic substances will lead to an increase in the development of cancer-related diseases and increased costs to treat them. [1]

Recent advances in cancer therapy have improved patient outcomes through better prevention methods, diagnostic tools, and treatment options. However, some cancer therapeutics still lack effective and targeted treatment. [2] Nanocarriers in cancer therapy have gained attention due to their potential to enhance efficacy while reducing toxicity of anticancer drugs and providing targeted treatment. [3, 4] This work proposes a hybrid nanocarrier formulation that combines the advantages of 2D nanomaterials and polymer nanoparticles for cancer treatment. Nanosized graphene, specially reduced graphene oxide (rGO), has ideal photo properties and stability for photothermal therapy (PTT). [5] PTT is a non-invasive, targeted treatment that uses mild temperature increases (39–45 °C) to induce cancer cell death. PTT has been used to enhance radiotherapy and chemotherapy effects. [6] Furthermore, the aromatic rings present in rGO facilitate the delivery of drugs being capable of forming Pi-Pi interactions. However, rGO lacks the desired water stability of graphene oxide to be useful in biomedical applications. [7]

Nanoparticles (NP) composed of poly(lactic-co-glycolic acid) (PLGA), an FDA-approved co-polymer, present high biocompatibility and can biodegrade. The polymer degrades by cleaving into monomers of lactic and glycolic acids, and releases the content entrapped in the matrix in a timely and controlled manner. [8] PLGA NP can be produced by the method of nanoprecipitation (NanoP) to encapsulate hydrophobic drugs and water-oil-water double-emulsion (WOW) to encapsulate hydrophilic drugs. PLGA NanoP formulations were used to encapsulate Tegafur (TAF), and PLGA WOW formulations 5-Fluorouracil (5-FU). Tegafur is converted to 5-FU after metabolization. 5-FU and TAF are used in cancer treatments with other drugs like leucovorin, irinotecan, and oxaliplatin in conjunction. [9]

The production of rGO was made by chemical exfoliation of graphite using the modified Hummers method, ultrasonication to reduce the lateral size. Afterwards, a photoreduction method was used to obtain rGO. In NanoP, PLGA and rGO were dissolved in acetone, and added drop-by-drop to a water solution with emulsifier stabilizer polyvinyl alcohol (PVA) and Polyethyleneimine (PEI), under magnetic stirring. In WOW rGO and 5-FU were in water and were added drop-by-drop to the acetone solution containing PLGA, under tip sonication. Immediately, the resulting emulsion was poured to the water phase with the stabilizer PVA and

PEI, under magnetic stirring. After 2 h stirring, successive centrifugations were performed to remove excess PVA and PEI, and some aggregates.

Particle size, polydispersity index (PdI), surface charge, of rGO and different PLGA formulations were estimated using dynamic light scattering (DLS). Encapsulation efficiency (EE) of TAF and 5-FU were determined using a UV-Vis spectrophotometer and a standard calibration curve of each drug in ultra-pure water. The supernatant collected from centrifugations of blank formulations and with encapsulated drug allow to determine the drug present in the supernatant, EE can then be calculated with the following equation.

$$EE\ (\%) = (1 - \text{Detected free drug/theoretical amount added}) \times 100$$

The PTT potential was determined using a custom-built NIR (808 nm) LED system. PLGA-rGO dispersions were treated for 30 min at different power sets, 550 mW cm-2 for NanoP formulations and 1100 mW cm-2 for WOW formulations. The assay occurred inside an incubator at 37 °C. PLGA-rGO NP dispersions were prepared at different concentrations (100-500 µg mL-1), and the temperature increase was compared against ultrapure water (ΔT). Temperature readings were taken using a thermocouple probes system. Materials morphology and size were observed by transmission electron microscopy (TEM).

The rGO after ultrasonication presented average lateral dimensions <200 nm in TEM and surface charges of -37.8 ±1.2 mV (pH 7) using DLS. In NanoP, PLGA-rGO-NanoP presented sizes of 243.7 ± 3.9 nm with a PDI of 0.146 and surface charges of +35.1 ± 0.6 mV (pH 7). PLGA-rGO-NanoP-TAF had their size changed due the loading of TAF and presented sizes of 200.3 ± 1.0 nm with a PDI of 0.184 and surface charges of +26.4 ± 1.2 mV (pH 7). The encapsulation efficiency (EE) of TAF in PLGA-rGO-NanoP was of 80%. The EE in PLGA-rGO-NanoP was as expected due to the pi-pi interactions of rGO achieving a higher retention of 5-FU, a formulation with TAF and PLGA, in the same conditions with no presence of rGO, only had an EE of 30%. Photothermal potential of PLGA-rGO-NanoP dispersions achieved an ΔT of 10 °C after 30 mins. In WOW method the NP of PLGA-rGO-WOW presented sizes of 238.5 ± 0.5 nm with a PDI of 0. 164 and surface charges of +35.8 ± 0.6 mV (pH 7). The encapsulation of 5-FU in the PLGA-rGO-WOW-FU resulted in sizes of 258.4 ± 5.1 nm with a PDI of 0.235 and surface charges of +47.9 ± 0.7 mV (pH 7). The EE in PLGA-rGO-WOW-FU was 60%. PLGA-rGO-WOW dispersions achieved an ΔT of 14 °C. rGO incorporation in PLGA NP was confirmed by TEM, as shown in figure 1.

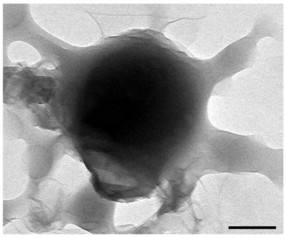

Figure 1. TEM image of PLGA-rGO. rGO is seen in between the matrix of the particle as well surrounding the particles due to the presence of PEI.

So far, rGO has been integrated in the PLGA NP using both tested methods. The potential of this new platform is interesting due to the combination of a drug carrier with the photothermal capabilities. Further work is necessary in cell culture to evaluate biocompatibility, bioactivity, and also to determine drug release kinetics of the nanoparticles. Also, the ideal glass-transition temperature of PLGA can allow for the release on-demand of the encapsulated drugs. In conclusion, these early results are promising regarding the final goal of formulating a drug delivery system that can be combined with phototherapy both to promote controlled drug release and for a synergistic effect for cancer therapy.

References:

1. Ferlay, J., et al., Estimating the global cancer incidence and mortality in 2018: GLOBOCAN sources and methods. Int J Cancer, 2019. 144(8): p. 1941-1953.

2. Tarantino, P., et al., Immunotherapy for early triple negative breast cancer: research agenda for the next decade. NPJ Breast Cancer, 2022. 8(1): p. 23.

3. Rosenblum, D., et al., Progress and challenges towards targeted delivery of cancer therapeutics. Nat Commun, 2018. 9(1): p. 1410.

4. May, M., Why drug delivery is the key to new medicines. Nat Med, 2022. 28(6): p. 1100-1102.

5. Amaral, S.I., et al., Carbon nanomaterials for phototherapy of cancer and microbial infections. Carbon, 2022. 190: p. 194-244.

6. Ferreira, L.P., et al., Screening of dual chemo-photothermal cellular nanotherapies in organotypic breast cancer 3D spheroids. J Control Release, 2021. 331: p. 85-102.

7. Azevedo, S., et al., Advances in carbon nanomaterials for immunotherapy. Applied Materials Today, 2022. 27.

8. Freitas, B., et al., Self-Assembled Bioactive Colloidal Gels as Injectable Multiparticle Shedding Platforms. ACS Applied Materials & Interfaces, 2020. 12(28): p. 31282-31291.

9. Bajetta, E., et al., Uracil/ftorafur/leucovorin combined with irinotecan (TEGAFIRI) or oxaliplatin (TEGAFOX) as first-line treatment for metastatic colorectal cancer patients: results of randomised phase II study. Br J Cancer, 2007. 96(3): p. 439-44.

Acknowledgments:

This work was financially supported by LA/P/0045/2020 (ALiCE), UIDB/00511/2020 and UIDP/00511/2020 (LEPABE), funded by national funds through FCT/MCTES (PIDDAC), base UIDB/04293/2020 Funding of the Institute for Research and Innovation in Health—i3S. This work is financially supported by national funds through the FCT/MCTES (PIDDAC), under the UT Austin PT Program, under the project UTAP-EXPL/NPN/0044/2021—2D-Therapy, also under the FCT project 2022.04494.PTDC—PhotoRect. Project 2SMART—engineered Smart materials for Smart citizens, with reference NORTE-01-0145-FEDER-000054, supported by Norte Portugal Regional Operational Programme (NORTE 2020), under the PORTUGAL 2020 Partnership Agreement, through the European Regional Development Fund (ERDF). Artur Pinto thanks the Portuguese Foundation for Science and Technology (FCT) for the financial support of his work contract through the Scientific Employment Stimulus—Individual Call—(CEECIND/03908/2017).

380Combining 3D Models of Anatomical and Thermal Images

Catarina Lopes[1], Adelio Vilaca[2], Cristina Santos[3], Joaquim Mendes[1,*]

[1]Faculty of Engineering, University of Porto, Rua Dr. Roberto Frias, 4200-465 Porto, Portugal, and Institute of Science and Innovation in Mechanical and Industrial Engineering, Associated Laboratory for Energy, Transports and Aeronautics, Rua Dr. Roberto Frias 400, 4200-465 Porto, Portugal

[2]Department of Orthopaedics, Centro Hospitalar Universitário de Santo António, Largo do Professor Abel Salazar, 4099-001 Porto, Portugal, and Abel Salazar Biomedical Sciences Institute, University of Porto, Rua Jorge de Viterbo Ferreira, 4050-313 Porto, Portugal

[3]Center for MicroElectroMechanical Systems, University of Minho, Campus of Azurém, Avenida da Universidade, 4800-058 Guimarães, Portugal, and Associate Laboratory in Biotechnology and Bioengineering and Microelectromechanical Systems, University of Minho, Campus of Gualtar, Rua da Universidade, 4710-057 Braga, Portugal

*Correspondence: jgabriel@fe.up.pt

Author Keywords: 3D Image Reconstruction, 3D Image Visualisation, 3D Modelling, Knee Joint, Medical Imaging, Thermal Imaging

Introduction: Computed tomography (CT) and magnetic resonance imaging (MRI) are the gold standard medical imaging systems in preclinical research. Both imaging modalities provide inner information regarding the anatomy of the human body by creating a set of sectioned image slices that can be reconstructed into three-dimensional (3D) models [1]. By tackling different anatomy structures, both have been common approaches for pre- or intra-operative image technology, having been reported has reliable and accurate, assisting physicians with a visual representation of reality [2-4]. However, they are solely based on the patient's anatomy, so a novelty approach, involving the combination of anatomical (CT/MRI) and functional (thermography) models, has recently started being explored [5, 6].

Moreover, thermography is being used as a complementary imaging technique for diagnosis and monitoring of pathologies. This is due to both the advances in infrared sensors in recent years, and the fact that thermal variations of the human body may indicate the existence of abnormalities, such as inflammation and infection [7]. Thus, combining this physiological information with the anatomical information of medical imaging modalities is of great relevance to the medical community.

Methods: The patient underwent the clinical protocol for acquisition of anatomical images of the left knee, in this case CT and MRI. The 3D Slicer software was used for pre-processing and model computation of the images. After the import of the DICOM data, and visualisation and selection of the ones with focus on knees, the image sets for each modality were chosen. This was followed by determining the delimitations of the left knee. The images were piled up and connected automatically generating a 3D anatomical model, that contains 3D inner information based on CT/MRI data. Afterwards, to compute a 3D anatomical shell, the left knee was segmented, and a model was generated, presenting the outer 3D shell based on CT/MRI data. Once the model computation was finished, 3D anatomical shells were exported to the Blender software, where the surface was smoothed, having a closer appearance to the real-life knee.

Before the acquisition of the thermal data, the patient was undressed for approximately 15 minutes for an acclimatisation period. A 360º video was taken using a thermal camera (model FLIR E60), which was positioned on a Lego built tripod that fit perfectly onto a motorised Lego train track supported by boxes to provide height, whilst the patient was standing with the left leg inside the camera range and the other leg placed on a chair outside the camera range. The collected video was manipulated using the FLIR Tools software, having a simple black background with the Rainbow HC palette and defined temperature limits (23ºC-35ºC) to facilitate the pre-processing in the MATLAB software.

The thermal video was transformed into single frames. To improve the visual quality of thermal images and facilitate the 3D point cloud generation, an image intensification was done to each frame [8]. The SfM algorithm [9] was applied to these frames to compute a 3D point cloud, with the VisualSFM software [10]. SfM requires extraction of features in images and their matching between images; estimation of camera motion; and sparse reconstruction of a 3D point cloud using the estimated camera motion and features [9].

For reconstruction refinement, there can be an optimisation of the cameras positioning via bundle adjustment, followed by dense reconstruction to compute a dense and united 3D point cloud [5].

The cloud was used to wrap the thermal images around the 3D anatomical shell to create a 3D thermal shell, presenting the thermal information of the surface of the knee. This stage was performed with the MeshLab software, where a manual alignment of the 3D point cloud with the 3D anatomical shell was done by computing a 3D registration of both meshes, based on affine transformation. That means that there was a mapping and transformation of both meshes into a common coordinate system and similar scaling [5, 6]. After the alignment process, the projection of the thermal images onto the 3D anatomical shell was computed, based on the information given by the 3D point cloud. Thus, the 3D thermal shell was generated via raster mode, where thermal images were superimposed over the 3D anatomical model for inspection. Then, the respective value of the pixel in 3D was obtained depending on the distance of the point to the camera position and the distance to the centre of the thermal image [8].

The final model is the union of the 3D anatomical model, that contains the anatomical CT/MRI inner information in 3D provided by the DICOM images, and the 3D thermal model, that is composed of a 3D thermal shell, giving information regarding the outer temperature distribution. So, both models were imported into the 3D Slicer software for combined visualisation in a common coordinate system.

Results and Discussion: The 3D Slicer software allowed for visualisation of axial, coronal, and sagittal slicing of the multimodal model. With these views, it is then possible to inspect and evaluate at the same time the anatomical and functional parts of the knee, which can be quite relevant to the medical community. It has been proven that inflammation and infection can be detected using thermal imaging, thanks to local changes in temperature due to variations regarding blood supply and metabolism [11]. Thus, a correlation between the found inflammations and infection on the surface of the model and anatomical injuries has potential, for example, to improve the accuracy and precision of the surgical plan, by providing more information regarding the severity of pathologies. Besides, multimodal imaging could assist in tracking treatment progress, by analysing the recovery of bones and soft tissues alongside the progression of inflammation and infection [5, 6].

Apart from visualisation of both 3D multimodal models, 40 alignment markups were randomly spread all over each model, calculating the displacement error of each markup. For the CT data, there was an average alignment error of 1.65 mm, whereas for the MRI data, the average error was of 1.00 mm. The difference in these average errors was noticeable, due to the thermal model overlapping more with the MRI model than with the CT model. It is worth mentioning that the software allows for visualisation of each model individually in case the overlapping keeps the user from seeing the model where they intend to focus on.

The analysis was inspired by Krefer AG et al. [8], with the average error of 4.58 mm, and by Abreu de Souza M et al. [5], with an average error of 1.77 mm. This indicates that the proposed research was efficient since the displacement could be crucial when expanding this methodology to medical applications.

Conclusion: The proposed methodology presented the process of visualising a 3D multimodal model of the knee, that included anatomical imaging modalities, such as CT and MRI imaging, and a functional imaging modality, specifically thermal imaging. Throughout the research, computer vision software was used for the pre-processing of the images, and the 3D reconstruction and visualisation of all three modalities.

The paper showed results regarding the visualisation of the multimodal model, demonstrating that the combination of an anatomical model with a functional model could be of great importance for medicine, in particular for surgical planning and monitoring of pathologies. Each multimodal model was evaluated considering the displacement error between the 3D anatomical models and the 3D thermal model. The methodology proposed is considered reasonable, since it is not feasible for the CT/MRI imaging to be acquired at the same time as the thermal imaging. Moreover, it was seen as an expanding process to diagnosis, surgery, and follow-up care.

References:

[1] van Geuns RJM, Wielopolski PA, de Bruin HG, Rensing BJ, van Ooijen PMA, Hulshoff M, et al. Basic principles of magnetic resonance imaging. Progress in Cardiovascular Diseases. 1999 Sep 1;42(2):149–56.

[2] Picard F, Deakin AH, Riches PE, Deep K, Baines J. Computer assisted orthopaedic surgery: past, present and future. Medical Engineering and Physics. 2019 Oct 31;72:55–65.

[3] Pailhé R. Total knee arthroplasty: Latest robotics implantation techniques. Orthopaedics & Traumatology: Surgery & Research. 2021 Feb 1;107(1, Supplement):102780.

[4] Fernandes LR, Arce C, Martinho G, Campos JP, Meneghini RM. Accuracy, Reliability, and Repeatability of a Novel Artificial Intelligence Algorithm Converting Two-Dimensional Radiographs to Three-Dimensional Bone Models for Total Knee Arthroplasty. J Arthroplasty. 2022 Dec 9;S0883-5403(22)01062-2.

[5] Abreu de Souza M, Alka Cordeiro DC, Oliveira J de, Oliveira MFA de, Bonafini BL. 3D Multi-Modality Medical Imaging: Combining Anatomical and Infrared Thermal Images for 3D Reconstruction. Sensors. 2023 Jan;23(3):1610.

[6] Schollemann F, Barbosa Pereira C, Rosenhain S, Follmann A, Gremse F, Kiessling F, et al. An Anatomical Thermal 3D Model in Preclinical Research: Combining CT and Thermal Images. Sensors. 2021 Jan;21(4):1200.

[7] Diakides NA, Bronzino JD. Medical Infrared Imaging. Boca Raton: CRC Press; 2007. 448 p.

[8] Krefer AG, Lie MMI, Borba GB, Gamba HR, Lavarda MD, Abreu de Souza M. A method for generating 3D thermal models with decoupled acquisition. Computer Methods and Programs in Biomedicine. 2017 Nov 1;151:79–90.

[9] Özyeşil O, Voroninski V, Basri R, Singer A. A survey of structure from motion. Acta Numerica. 2017 May;26:305–64.

[10] Vacca G. OVERVIEW OF OPEN SOURCE SOFTWARE FOR CLOSE RANGE PHOTOGRAMMETRY. Int Arch Photogramm Remote Sens Spatial Inf Sci. 2019 Aug 23;XLII-4/W14:239–45.

[11] Całkosiński I, Dobrzyński M, Rosińczuk J, Dudek K, Chrószcz A, Fita K, et al. The use of infrared thermography as a rapid, quantitative, and noninvasive method for evaluation of inflammation response in different anatomical regions of rats. Biomed Res Int. 2015;2015:972535.

384Muscle coactivation analysis for neuromuscular control assessment of lower limb stretch-shortening cycle

Carlos Rodrigues[1,*], Miguel Correia[2], João Abrantes[3], Marco Benedetti[4], Jurandir Nadal[5]

[1]Doctoral Program in Biomedical Engineering, Faculdade de Engenharia, Universidade do Porto, Rua Dr. Roberto Frias, 4200-465 Porto, Portugal

[2]Department of Electrical and Computer Engineering, Faculdade de Engenharia, Universidade do Porto, Rua Dr. Roberto Frias, 4200-465 Porto, Portugal

[3]MovLab - Interactions and Interfaces Laboratory, Universidade Lusófona de Humanidades e Tecnologias, Campo Grande, 1749-024 Lisboa, Portugal

[4]Department of Electronic and Systems, Universidade Federal de Pernambuco, Cidade Universitária, 50670-901 Recife, Brasil

[5]Biomedical Engineering Program, Universidade Federal do Rio de Janeiro, Av. Horácio Macedo 2030, 21941-972 Rio de Janeiro, Brasil

*Correspondence: c.rodrigues@fe.up.pt

Author Keywords: Neuromuscular control, coactivation, stretch-shortening cycle.

Abstract

This study presents and applies muscle coactivation analysis based on subject specific surface electromyography (sEMG) of lower limb muscles during long, short and no stretch-shortening cycle (SSC) assessed on standard maximum vertical jump (MVJ) with countermovement jump (CMJ), drop jump (DJ) and squat jump (SJ). Performed analysis conducted to detection of different muscle coactivation pattern at each SSC pointing for distinct synergistic activity of mono and bi-articular muscles.

Introduction: Muscle stretch-shortening cycle (SSC) is a central mechanism with lower limb muscle contraction immediately preceded by muscle stretch for efficient submaximal activities such as gait and powerful maximal activities such as running and jumping (Zatsiorsky 2006; Komi, Ishikawa, and Linnamo 2011). Although muscle SSC can be observed at gait and running its higher expression and accessibility is performed on standard maximum vertical jump (MVJ) with an open issue on neuromuscular control assessment of lower limb muscle SSC (Bobbert 2002). For this purpose, we present and applied noninvasive subject specific analysis of lower limb muscle coactivation for selected muscles with higher contribution during MVJ impulse based on corresponding conditioned surface electromyographic signals (sEMG).

Methods: Selected muscles correspond to lower limb muscles vastus medialis (VM), rectus femoris (RF), vastus lateralis (VL), lateral gastrocnemius (LG) and medial gastrocnemius (MG) as schematically represented in Figure 1. Twenty-seven trials were assessed corresponding for each subject to the highest MVJ based on larger flight time with long SSC at countermovement jump (CMJ), short SSC at drop jump (DJ) and squat jump (SJ) with no SSC. Trial sample iscomposed by a group of six young adult volunteers' students on sports and physical education degree with the ages (21.5 ± 1.4) years, (76.7 ± 9.3) kg mass and (1.79 ± 0.06) m height. Surface skin was prepared and Aqua-Wet gel Skintact F55 electrodes were applied at bipolar configuration as indicated by SENIAN.

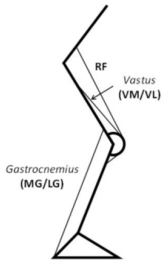

Figure 1: Line actions of rectus femoris (RF), vastus medialis (VM), vastus lateralis (VL), lateral gastrocnemius (LG) and medial gastrocnemius (MG) muscles.

After warmup each subject performed a total of three SJ, CMJ and DJ with sEMG data signal collected at 2000 Hz using wireless system Biotell 99 from Glonner Electronic GmbH. VM, RF, VL, LG and MG sEMG raw signal were normalized to maximum voluntary contraction (MVC), rectified and low-pass filtered with 5.0 Hz cut-off frequency second order Butterworth filter applied forward and backward to eliminate phase shift, obtaining sEMG linear envelope as presented on representative CMJ, DJ and SJ performed trials in Figure 2.

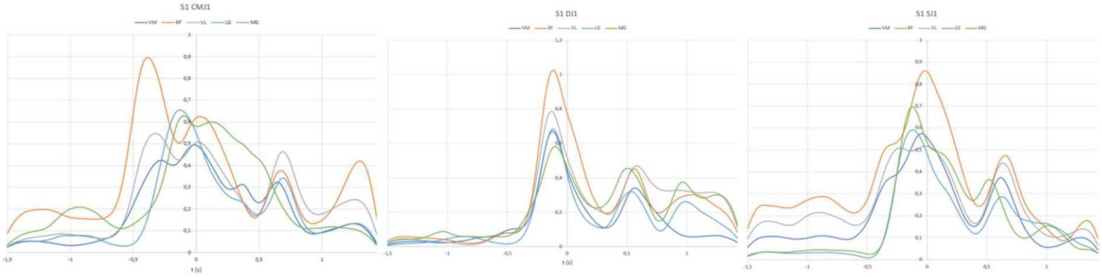

Figure 2: sEMG linear envelopes of vastus medialis (VM), rectus femoris (RF), vastus lateralis (VL), lateral gastrocnemius (LG) and medial gastrocnemius (MG) muscles at representative SJ, CMJ and DJ performed experimental trials

VM, RF, VL, LG and MG sEMG linear envelopes were paired plotted with the area under the curves computed as well as the coactivation pairs defined as the common area under the curves normalized to the sum of the corresponding pair individual areas under the curves. Coactivations were compared at CMJ, DJ and SJ as well as among CMJ, DJ and SJ.

Results: Strongest coactivations by decreasing intensity were detected between VM-RF and LG-MG muscles at CMJ and SJ, whereas at DJ the strongest coactivation was detected between LGMG and VL-MG as presented at Figure 3 and Table 1. Also, while the coactivations between quadriceps selected muscles VM-RF, VM-VL and RF-VL presented higher values at CMJ and SJ than DJ, the coactivations between the quadriceps selected muscles and the gastrocnemius presented higher values at CMJ and DJ than SJ as indicated in Table 1.

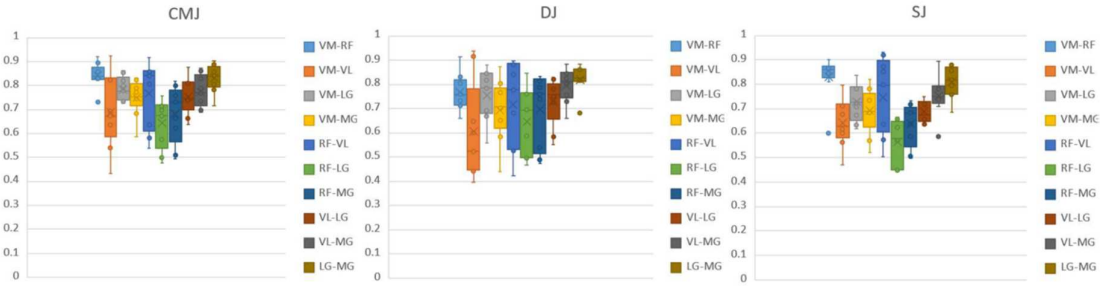

Figure 3: Boxplot of lower limb bi-articular muscles coactivations at CMJ, DJ and SJ

Table 1: Mean and standard deviation (Std) of lower limb bi-articular muscles coactivations (COACT) based onsEMG linear envelops during CMJ, DJ and SJ

COACT Mean (Std)	VM-RF	VM-VL	VM-LG	VM-MG	RF-VL	RF-LG	RF-MG	VL-LG	VL-MG	LG-MG
CMJ	0.843	0.690	0.785	0.748	0.766	0.644	0.682	0.754	0.775	0.831
	(0.053)	(0.154)	(0.051)	(0.075)	(0.141)	(0.101)	(0.118)	(0.075)	(0.068)	(0.058)
DJ	0.767	0.604	0.753	0.694	0.717	0.647	0.696	0.731	0.796	0.821
	(0.075)	(0.199)	(0.107)	(0.127)	(0.183)	(0.139)	(0.151)	(0.098)	(0.070)	(0.058)
SJ	0.832	0.643	0.728	0.692	0.747	0.564	0.637	0.688	0.753	0.810
	(0.090)	(0.097)	(0.077)	(0.095)	(0.160)	(0.092)	(0.089)	(0.044)	(0.082)	(0.067)

Discussion: Despite the strongest coactivation was detected at intramuscular group level, these muscular groups were distinct depending on MVJ type, with the highest coactivation of the selected quadriceps muscles detected at CMJ and SJ whereas the highest coactivations on DJ was detected at the gastrocnemius. Additionally, similar pattern arises on muscle coactivations at CMJ, DJ and SJ with higher values at CMJ than DJ and SJ for VM-RF, VM-VL, VM-LG, VM-MG and RF-VL whereas CMJ and DJ presented higher values than SJ at RF-LG, RF-MG, VL-LG, VLMG, and LG-MG.

Conclusion: Muscle coactivation based on sEMG linear envelope conduced to detection of different behavior of lower limb muscles at long, short and no SSC assessed on standard MVJ. Although attention was focused on large number of lower limb bi-articular muscles due to the ability of these muscles to perform considerable tension at limb transversal direction and thus to the transference of joint muscle power, coactivation proved to be an important complementary tool for detection of simultaneous activity of synergistic muscle action on SSC study, thus extending its application on antagonistic activity detection.

References:

Bobbert, M. 2002. "The Effect of Coordination on Vertical Jumping Performance". In K. E. Gianikellis (Ed.), Scientific Proceedings of the XXth International Symposium on Biomechanics in Sports, 355-361.

Zatsiorsky, V. M. 2006. "Task-Specific Strength". In Science and Practice of Strength Training, 14-32. Heidelberg: Springer.

Komi, P.V., Ishikawa, M. and Linnamo, V. 2011. "Identification of Stretch-Shortening Cycles in Different Sports". Portuguese Journal of Sport Sciences 11 (Suppl. 2):529-551.

Posters to be displayed in the Symposium

Poster 01

Chlorhexidine-releasing composite hydrogel for the prevention and control of bacterial infections
Ana Luísa Fernandes, Maria Tavares, Liliana Grenho, Joana Barros

Poster 02

A 3D Computational Framework for Simulating Cell Proliferation
Maria Inês Barbosa, Jorge Belinha, Renato Natal Jorge, Ana Carvalho

Poster 03

Sagittal lower limb joint angular kinematic coordination at different standard maximum vertical jump
Carlos Rodrigues, Miguel Correia, João Abrantes, Marco Benedetti, Jurandir Nadal

Poster 04

Development of bioceramic porous microspheres for bone regeneration
Catarina Costa Reis, Miguel Ângelo Rodrigues, José Domingos Santos, Maria Ascensão Lopes

107Chlorhexidine-releasing composite hydrogel for the prevention and control of bacterial infections

Ana Luísa Fernandes[1,3], Maria Tavares[1], Liliana Grenho[3], Joana Barros[2,*]

[1]Faculdade de Engenharia, Universidade do Porto, Rua Dr. Roberto Frias, 4200-465 Porto, Portugal

[2]i3S, Rua Alfredo Allen, Porto, Portugal

[3]Faculdade de Medicina Dentária, Universidade do Porto, Rua Dr. Manuel Pereira da Silva, 4200-393 Porto, Portugal

*Correspondence: joana.barros@ineb.up.pt

Author Keywords: Biomaterial, Chlorhexidine, Hydrogel, Implant-related infections.

Extended Abstract

The emergence of bacterial infections following the implantation of biomaterialbased bone implants has substantially impacted patients' quality of life and placed a strain on healthcare systems [1,2]. Biomaterials loaded with antibiotics have been used as vehicles for the local delivery of antimicrobial agents to prevent, control and treat implant-related infections (IRIs) [3-5]. However, antibiotic resistance is an acute concern to the global community, being required an alternative antimicrobial agent to control and treat IRIs, particularly those caused by antibiotic-resistant bacteria. Chlorhexidine (CHX) has been described as a good candidate for the development of multifunctional approaches based on anti-infective biomaterials and drug-delivery systems that do not encourage microbial evolution, similar to antibiotic resistance [5-7]. This antiseptic has a wide-spectrum antibacterial activity, acting against Gramnegative and Gram-positive bacteria, bacterial spores, lipophilic viruses, yeast, and dermatophytes [8]. In addition to low drug resistance, CHX presents good soft tissue tolerability, hence being used in biomedical applications like controlled drug delivery in dental medicine [1]. Therefore, the present work intends to develop CHX-loaded alginate-nanohydroxyapatite composite hydrogels to prevent local tissue infections and, simultaneously, to promote bone tissue regeneration. A physicochemical (swelling, FTIR, SEM) and biological (halo of inhibition test) characterization of the materials was performed. The obtained results showed that the materials have a porous structure with good swelling behaviour and their functional groups were identified; the halo of inhibition test showed that the process of production did not affect the CHX's bioactivity. At the end of this work, a multifunctional biomaterial integrating osteogenic and antibacterial functions is expected to support bone cells' osteogenic functions and prevent bacterial colonization.

References:

[1] Zhao, C., Liu, W., Zhu, M., Wu, C., & Zhu, Y. (2022). Bioceramic-based scaffolds with antibacterial function for bone tissue engineering: A review. Bioactive Materials.

[2] Ribeiro, M., Monteiro, F. J., & Ferraz, M. P. (2012). Infection of orthopaedic implants with emphasis on bacterial adhesion process and techniques used in studying bacterial-material interactions. Biomatter, 2(4), 176-194.

[3] Benedini, L., Laiuppa, J., Santillán, G., Baldini, M., & Messina, P. (2020). Antibacterial alginate/nano-hydroxyapatite composites for bone tissue engineering: Assessment of their bioactivity, biocompatibility, and antibacterial activity. Materials Science and Engineering: C, 115, 111101. 1

[4] Barros, J. A. R., de Melo, L. D. R., da Silva, R. A. R., Ferraz, M. P., de Rodrigues Azeredo, J. C. V., de Carvalho Pinheiro, V. M., ... & Monteiro, F. J. (2020). Encapsulated bacteriophages in alginate-nanohydroxyapatite hydrogel as a novel delivery system to prevent orthopedic implant-associated infections. Nanomedicine: Nanotechnology, Biology and Medicine, 24, 102145.

[5] Riool, M., Dirks, A. J., Jaspers, V., de Boer, L., Loontjens, T. J., van der Loos, C. M., ... & Zaat, S. A. (2017). A chlorhexidine-releasing epoxy-based coating on titanium implants prevents Staphylococcus aureus experimental biomaterial-associated infection. Eur Cell Mater, 33, 143-157.

[6] Wang S, Yang Y, Li W, Wu Z, Li J, Xu K, et al. Study of the Relationship Between Chlorhexidine-Grafted Amount and Biological Performances of Micro/Nanoporous Titanium Surfaces. ACS Omega. 2019;4:18370-80.

[7] Barros J, Grenho L, Fontenente S, Manuel CM, Nunes OC, Melo LF, et al. Staphylococcus aureus and Escherichia coli dual-species biofilms on nanohydroxyapatite loaded with CHX or ZnO nanoparticles. Journal of biomedical materials research Part A. 2017;105:491-7.

[8] Barros, J., Grenho, L., Fernandes, M. H., Manuel, C. M., Melo, L. F., Nunes, O. C., ... & Ferraz, M. P. (2015). Anti-sessile bacterial and cytocompatibility properties of CHX-loaded nanohydroxyapatite. Colloids and Surfaces B: Biointerfaces, 130, 305- 314.

112A 3D Computational Framework for Simulating Cell Proliferation

Maria Inês Barbosa[1], Jorge Belinha[2], Renato Natal Jorge[3], Ana Carvalho[4]

[1]Instituto de Ciência e Inovação em Engenharia Mecânica e Engenharia Industrial, Campus da FEUP, R. Dr. Roberto Frias 400, 4200-465 Porto, Portugal

[2]Departamento de Engenharia Mecânica, Instituto Superior de Engenharia do Porto, R. Dr. António Bernardino de Almeida 431, 4249-015 Porto, Portugal

[3]Departamento de Engenharia Mecânica, Faculdade de Engenharia, Universidade do Porto, Rua Dr. Roberto Frias, 4200-465 Porto, Portugal

[4]Instituto de Investigação e Inovação em Saúde, R. Alfredo Allen 208, 4200-135 Porto, Portugal

*Correspondence: anacarvalho@ibmc.up.pt

Author Keywords: Numerical Simulation, Particle Method, Cell Proliferation, Cell Growth, Cell Division.

Abstract

Cell proliferation is a complex and crucial function of cells, as a balance between cell proliferation and apoptosis is necessary to maintain homeostasis and a healthy human body. Along with traditional experimental studies, computational models and simulations are considered valuable tools in advancing research on cell proliferation and other biological processes. This study proposes a novel algorithm for simulating the process of cell proliferation, and it was created in order to be solved by a particle meshless method (the Smoothed Particle Hydrodynamics). To verify the effectiveness of the algorithm, it was calibrated and validated under different numerical analyses, studying individual cells and groups of cells. The analyses looked at volume growth, reproducibility, and for cell groups, the diameter, volume, and shape of the cluster. At the end of this work, the algorithm was able to simulate the processes of cell growth and division. An exponential growth in the number of cells was obtained, and all simulations produced logical and similar results.

Introduction:

Cell proliferation is the process of cell growth followed by division into two new genetically identical cells (Tortora and Derrickson 2017, Standring 2015). This process is essential in situations that cause cell damage and is necessary to maintain the natural balance of the human body (Sandal 2002, Cristini and Lowengrub 2010).

Mathematical and computational models have been used to aid research in this field, allowing for faster predictions and exploration of new paths at a lower cost (Banerjee 2021). However, the available models are still unable to fully replicate the all process because of its huge complexity (Ingolia and Murray 2004).

Different numerical methods have been applied to solve and study these models. The Smoothed Particle Hydrodynamics (SPH) method is currently one of the most popular methods used to performed computer simulations since it is quite simple and robust when performing kernel integration (Liu and Liu 2003, Monaghan 1992).

The goal of this work was to develop a new 3D non-linear iterative algorithm that uses SPH and the Navier-Stokes equations to simulate the process of cell proliferation. The algorithm was designed to mimic the process of cells proliferation and so, it includes the growth and division of cells. To study and verify the how the algorithm works, different analyses were conducted. In these, the growth along the iteration for cells and the diameter, volume, and shape of the clusters were considered.

Methods:

The proposed algorithm simulates the process of cell proliferation and it is solved by the SPH method. This method involves discretizing the domain using particles, in which the relationship between them is not known, and an integral representation that generates approximation functions to approximate the field function. The Navier-Stokes equations are then solved using these functions, and particle approximation happens iteratively (Liu and Liu, 2003).

To start the algorithm, initial input data is defined to create particle discretization. For this study, three types of particles were assumed, with one particle initially defined as a cell in the centre of the domain. The initial velocity, internal pressure, and acceleration were then calculated for the entire domain. Afterward, the cell is allowed to grow and its growth continues until the cell doubles its initial volume. Once this occurs, the process of division is initiated and two cells are created. In result, a new particle is added to the domain. This process is then repeated by the two new cells. It is worth noting that kernel functions are generated in each iteration, and the position of the particles is updated based on them.

Results and Discussion:

Various analyses were conducted to see the efficiency of the algorithm and to calibrate it. These analyses included considering seven cell divisions and running twenty simulations. The growth of the cells and the form, volume, and diameter of the cell clusters obtained during the evolution of the process were examined until the seventh division occurred. This pattern repeated for the two new cells and in the next cell divisions, resulting in an exponential increase in the number of cells along the simulations. Furthermore, the main difference between the clusters of cells was in the position of the cells. Despite that, the results were quite similar, as well as in terms of shape, diameters and volumes.

Conclusions:

Based on the results of the various simulations performed, the process of cell proliferation of a single cell and a group of cells was possible to be simulated using the proposed algorithm, showing its efficiency and robustness. The results were appropriate and consistent with the natural growth pattern of cells in vivo and with the data described in the literature. Furthermore, despite the randomness associated with the algorithm, the different simulations demonstrated its reproducibility.

Although still in its early stages, overall, the proposed algorithm seems to be a promising tool for studying the process of cell proliferation and should be further explored. Future work could include different improvements to produce more complex and realistic simulations. For instance, extracellular factors that influence the proliferation process could be introduced to the model.

References:

Tortora, G. J. and B. H. Derrickson. 2017. "Introduction to the human body". John Wiley & Sons, Incorporated.

Standring, S. 2015. "Gray's anatomy e-book: the anatomical basis of clinical practice". Elsevier Health Sciences.

Sandal, T. 2002. "Molecular aspects of the mammalian cell cycle and cancer". The oncologist 7(1): 73-81.

Cristini, V. and J. Lowengrub. 2010. "Multiscale modeling of cancer: an integrated experimental and mathematical modeling approach". Cambridge University Press.

Banerjee, S. 2021. "Mathematical modeling: models, analysis and applications". Chapman and Hall/CRC.

Ingolia, N. T. and A. W. Murray. 2004. "The ups and downs of modeling the cell cycle". Current Biology 14(18): R771-R777.

Liu, G. R. and M. B. Liu. 2003. "Smoothed particle hydrodynamics: a meshfree particle method". World scientific.

Monaghan, J. J. 1992. "Smoothed particle hydrodynamics". Annual review of astronomy and astrophysics 30: 543-574.

Acknowledgments

The authors truly acknowledge the funding provided by Ministério da Ciência, Tecnologia e Ensino Superior - Fundação para a Ciência e a Tecnologia (Portugal), under the Grant SFRH/BD/146272/2019. Additionally, the authors acknowledge the funding provided by LAETA, under the project UIDB/50022/2020.

385Sagittal lower limb joint angular kinematic coordination at different standard maximum vertical jump

Carlos Rodrigues[1,*], Miguel Correia[2], João Abrantes[3], Marco Benedetti[4], Jurandir Nadal[5]

[1]Doctoral Program in Biomedical Engineering, Faculdade de Engenharia, Universidade do Porto, Rua Dr. Roberto Frias, 4200-465 Porto, Portugal

[2]Department of Electrical and Computer Engineering, Faculdade de Engenharia, Universidade do Porto, Rua Dr. Roberto Frias, 4200-465 Porto, Portugal

[3]MovLab - Interactions and Interfaces Laboratory, Universidade Lusófona de Humanidades e Tecnologias, Campo Grande, 1749-024 Lisboa, Portugal

[4]Department of Electronic and Systems, Universidade Federal de Pernambuco, Cidade Universitária, 50670-901 Recife, Brasil

[5]Biomedical Engineering Program, Universidade Federal do Rio de Janeiro, Av. Horácio Macedo 2030, 21941-972 Rio de Janeiro, Brasil

*Correspondence: c.rodrigues@fe.up.pt

Author Keywords: Lower limb, joint angular kinematics, coordination.

Extended Abstract

This study presents and applies cross-correlation (CCr) analysis and time delay of maximum CCr for coordination assessment of sagittal lower limb joint angular displacements, velocities, and accelerations during impulse phase at different standard maximum vertical jump (MVJ) with long, short and no countermovement (CM) and muscle stretch-shortening cycle (SSC). Fifty-four subject specific noninvasive experimental trials were assessed performed by a group of six volunteers' students of sports and physical education degree and different pattern was detected for time delay of maximum CCr at the hip, knee, and the ankle joints.

Introduction: Standard maximum vertical jump (MVJ) has been applied with long countermovement (CM) on countermovement jump (CMJ) and short CM on drop jump (DJ) for comparison to squat jump (SJ) and no CM (Bobbert 1987) and muscle stretch-shortening cycle (SSC), Zatsiorsky (2006) and Komi (2011). With muscle groups acting multiple joints and joints acted by several muscle groups, lower limb joint angular coordination plays a central role on understanding multiple joint movement at complex movements such as standard MVJ (Bobbert 1988, 2002). With time integration of joint acceleration produced by muscle forces, lower limb joint angular velocities are prone to time delay with the same for joint angular displacements resulting from time integration of joint angular velocities. Nevertheless, joint angular coordination assessment at different standard MVJ requires entire time series analysis of kinematic signals, avoiding single point subjective analysis to access coordination. For this reason, we applied cross correlation (CCr) of the hip (H), the knee (K) and the ankle (A) joint angular accelerations (α), velocities (ω) and displacements (Θ) to assess maximum CCr (CCr_max) and time delay (τ) of the kinematic signal wave propagation determining lower limb joint MVJ coordination.

Methods: Fifty-four experimental trials were assessed, performed by a group of six volunteers' students of sports and physical education degree with ages (21.5 ± 1.4) years, (76.7 ± 9.3) kg mass and (1.79 ± 0.06) m height. Subjects wear skin surface reflective markers at palped right and left acromion's, anterior superior iliac spines, femoral epicondyles, malleolus, tibial tubercles, and heads of the 5th metatarsals. Each subject performed a total of 3 SJ, 3 CMJ and 3 DJ trials. Images were acquired with two JVC GR-VL9800 cameras parallel to the sagittal plane with 3D markers cartesian coordinates obtained from direct linear transformation (DLT) tracking with Simi Motion 6.1 as depicted in Figure 1.

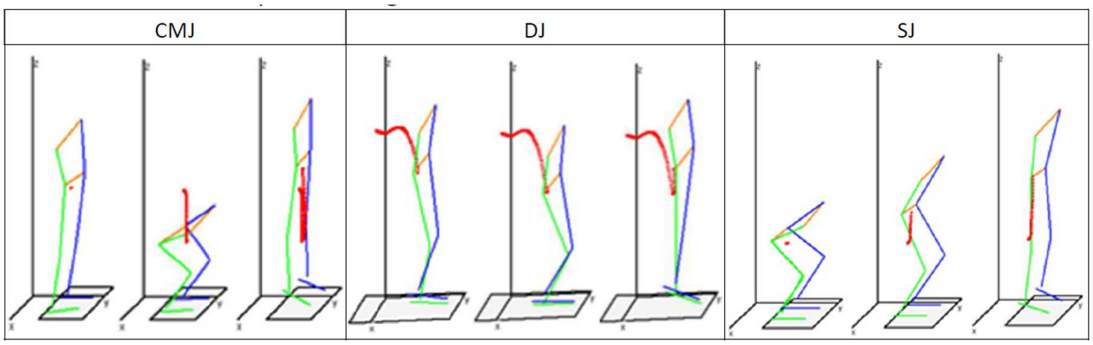

Figure 1: Lower limb and torso stick-figures at the start, the middle and the end of the impulse phase during CMJ, DJ and SJ performed experimental trials

Best SJ, CMJ and DJ trials were selected for each subject based on higher flight time and inverse-kinematics was performed obtaining the hip, the knee and the ankle sagittal angular displacements, velocities, and accelerations on representative CMJ, DJ and SJ performed trials. Angular displacements (Θ) were cross-correlated (CCr) with angular velocities (ω) and angular accelerations (α) for the hip (H), the knee (K) and the ankle (A).

Results: SJ presented strongest cross-correlation CCr(Θ,ω) than DJ, both with higher maximum values CCr_max at the hip (H) than the knee (K) and the ankle (A), whereas CMJ presented opposite higher values at the ankle than the knee and the hip, as presented on Table 1 and Figure 2. Regarding joint angular velocity (ω) and acceleration (α) cross-correlation, SJ presented higher CCr(ω, α) values at the ankle than the knee and the hip, with the opposite at DJ higher CCr(ω, α) at the knee and the hip than the ankle, whereas CMJ presented higher CCr(ω, α) at the ankle than the hip and the knee. Comparatively CMJ, DJ and SJ presented similar relations of the joint angular displacement and acceleration cross-correlation CCr(Θ, α) with higher values at the ankle than the knee and the hip.

Table 1: Mean and standard deviation (Std) of the lower limb cross-correlation of the hip (H), knee (K) and the ankle (A) joint angular displacement, velocity and acceleration at CMJ, DJ and SJ

CCr_max	CMJ			DJ			SJ		
Mean (Std)	Hip	Knee	Ankle	Hip	Knee	Ankle	Hip	Knee	Ankle
CCr(θ,ω)	0.005	0.015	0.295	0.335	0.194	0.166	0.826	0.723	0.642
	(0.036)	(0.034)	(0.133)	(0.269)	(0.085)	(0.135)	(0.053)	(0.038)	(0.055)
CCr(ω,α)	0.573	0.552	0.833	0.684	0.703	0.667	0.567	0.765	0.882
	(0.130)	(0.121)	(0.083)	(0.205)	(0.131)	(0.068)	(0.128)	(0.125)	(0.044)
CCr(θ,α)	0.170	0.281	0.428	0.168	0.393	0.531	0.491	0.588	0.593
	(0.076)	(0.037)	(0.064)	(0.239)	(0.172)	(0.108)	(0.100)	(0.110)	(0.053)

Discussion: Whereas CMJ presented for CCr(Θ,ω) an inverse relation between CCr_max and corresponding time delay with higher τ at the hip than the knee and the ankle, DJ and SJ presented for CCr(Θ,ω) a similar relation between CCr_max and corresponding time delay with higher τ at the hip than the knee and the ankle, Table 1 and Figure 2. As regards to CCr(ω, α) opposite relation was detected at CMJ and SJ between CCr_max and corresponding time delay with higher τ at the hip than the knee and the ankle, whereas DJ presented similar relation of CCr_max and time delay with higher at the knee and the hip than the ankle. Finally, CCr(Θ, α) presented at CMJ, DJ and SJ simillar oposite relation between CCr_max and corresponding time delay with higher τ at the hip than the knee and the ankle.

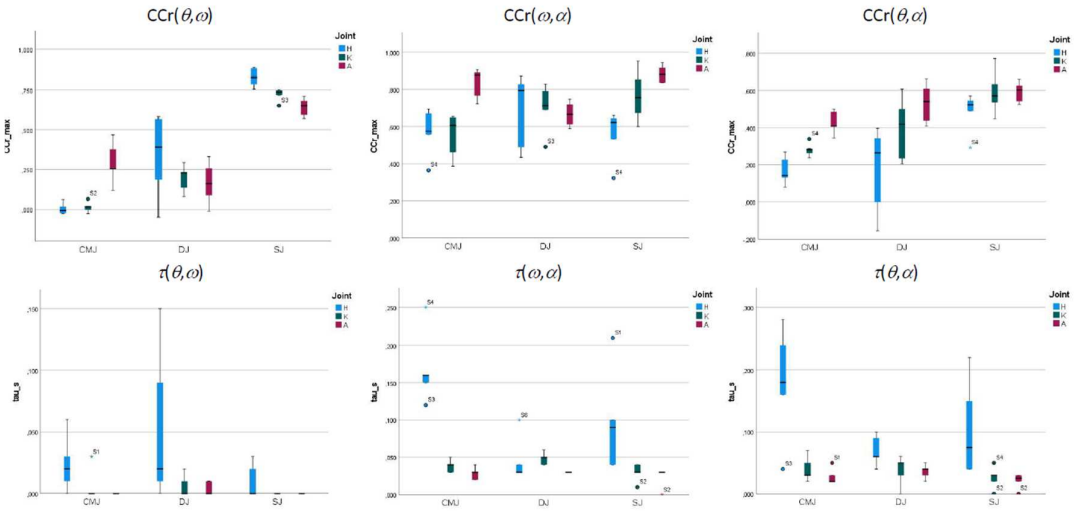

Figure 2: Lower limb maximum cross-correlation (CCr) and time delay for the hip(H), knee (K) and the ankle (A) sagittal joint angular displacement, velocity and acceleration at CMJ, DJ and SJ

Conclusion: Cross correlation of sagittal lower limb joint angular kinematics conduced to detection of different time delays of entire time series maximum CCr at the hip, the knee and the ankle angular displacements, velocities and accelerations on each MVJ type with long, short, no CM.

References:

Bobbert, M.F., Gerritsen, K.G.M., Litjens, M.C.A. and Van Soest, A.J. 1987. "Drop jumping. I. The influence of jumping technique on the biomechanics of jumping ". Medicine and Science in Sports and Exercise 19 (4):332–338.

Bobbert, M.F. and Van Ingen Schenau, G.J. 1988. "Coordination in Vertical Jumping". Journal of Biomechanics 21 (3):249–262.

Bobbert, M. 2002. "The Effect of Coordination on Vertical Jumping Performance". In K. E.

Gianikellis (Ed.), Scientific Proceedings of the XXth International Symposium on Biomechanics in Sports, 355-361.

Zatsiorsky, V. M. 2006. "Task-Specific Strength". In Science and Practice of Strength Training, 14-32. Heidelberg: Springer.

Komi, P.V., Ishikawa, M. and Linnamo, V. 2011. "Identification of Stretch-Shortening Cycles in Different Sports". Portuguese Journal of Sport Sciences 11 (Suppl. 2):529-551.

333Development of bioceramic porous microspheres for bone regeneration

Catarina Costa Reis, Miguel Ângelo Rodrigues, José Domingos Santos, Maria Ascensão Lopes*

LAQV-REQUIMTE, Department of Metallurgical and Materials Engineering, Faculty of Engineering, University of Porto, Porto, 4200-465, Portugal

*Correspondence: malopes@fe.up.pt

Author Keywords: Beta-tricalcium phosphate, bioceramic, biphasic calcium phosphate, bone, hydroxyapatite, synthetic biomaterial.

Introduction: With the increase in average life expectancy and consequent ageing of the population, there is an increase in the risk of fracture and a decrease in the capacity for bone healing and regeneration [1, 2]. Over the past few decades, there has been a significant increase in the development of synthetic biomaterials for bone applications to overcome the limitations associated with autografts, allografts and xenografts (e.g. rejection, infection and transmission of diseases). Bioceramics stand out due to their biocompatibility and mechanical properties (compressive strength, stiffness and fracture toughness), and the supply is not limited [3-6].

Among the most clinically used bioceramics in treating bone defects, synthetic biomaterials based on calcium phosphate, particularly biphasic calcium phosphate (BCP), stand out. BCP is a hydroxyapatite (HA) and beta-tricalcium phosphate (β-TCP) mixture. HA is used due to its similarity to the mineral phase of bone tissue; however, due to its low biodegradation rate, it can be associated with a more biodegradable phase, namely, β-TCP. So, this combination is advantageous due to the possibility of manipulating the proportion of the HA and β-TCP to optimise the biodegradation rate and consequently allow for a slow or a fast bone remodelling according to the specific application [7-10].

Porosity, the percentage of pores in a solid, is one of the properties to consider while developing materials for bone applications. A porous material may have closed (isolated) and open (interconnected) pores. The surface area of open porous materials is much higher, guaranteeing good mechanical fixation and providing sites on the surface that allow chemical bonding between bioceramics and bone tissue. In addition, the interconnected pores can transport drugs (to promote bone tissue growth, treat pathologies and prevent infections) [11].

This work aims to develop porous biphasic bioceramic spheres of different hydroxyapatite and beta-tricalcium phosphate ratios that will allow for drug delivery in the scope of bone regeneration.

Methods:

Production of bioceramic porous microspheres

First, bioceramic powders (hydroxyapatite and beta-tricalcium phosphate) were mixed with sodium alginate solution to make a ceramic suspension. Then, Pluronic F-127 surfactant was added to the ceramic suspension to obtain a ceramic foam. Spheres were obtained by injection into a calcium chloride solution and, after that, were submitted to a thermal treatment where the combustion of the organic material and the sintering of the bioceramics occurred.

Characterisation of bioceramic porous microspheres

To analyze the morphology of the samples (i.e. size and whether they are spherical), the stereomicroscope was used. Thus, this equipment had the function of quality control of the production of the spheres. Moreover, to analyze the morphology of the samples (i.e. size, whether they are spherical and qualify porosity) with high resolution, a scanning electron microscope (SEM) was used. X-ray diffraction (XRD) aimed to identify the crystalline phases present in the spheres. By comparing the positions of the peaks and their intensities with the databases provided, it was possible to verify the proportion of HA and TCP that the spheres had. Finally, to quantify the porosity of the spheres, the Archimedes principle was used.

Results and discussion: After analysing the size of the spheres before and after their sintering by stereomicroscope, the linear contraction results were between 20 and 30% and volumetric contraction results were between 50 e 60%. From these results, it was possible to calculate the size that the non-sintered

spheres should present to obtain sintered spheres with the desired size for a specific clinical purpose. In this way, linear and volumetric contraction were factors for customising bioceramic spheres. The spheres had an open porosity of above 70%, a closed porosity above 30%, and a total porosity above 70%. From these results, it was observed that the pores are primarily open (interconnected). Regarding XRD, it was observed that the HA and TCP in the spheres did not change phase because they are both pure phases.

Conclusions: It was possible to produce customisable HA and β-TCP porous microspheres that will allow for the incorporation and release of drugs according to the clinical needs in a bone regeneration context.

References:

[1] Maria Rosa Iaquinta et al. “Innovative biomaterials for bone regrowth”. In: International journal of molecular sciences 20.3 (2019), p. 618.

[2] Qixin Chen et al. “A multifunctional composite hydrogel that rescues the ROS microenvironment and guides the immune response for repair of osteoporotic bone defects”. In: Advanced Functional Materials 32.27 (2022), p. 2201067.

[3] Francesco Baino, Giorgia Novajra e Chiara Vitale-Brovarone. “Bioceramics and scaffolds: a winning combination for tissue engineering”. In: Frontiers in bioengineering and biotechnology 3 (2015), p. 202.

[4] Sergey V Dorozhkin. “Bioceramics of calcium orthophosphates”. In: Biomaterials 31.7 (2010), pp. 1465–1485.

[5] Zahid Abbas et al. “Toughening of bioceramic composites for bone regeneration”. In: Journal of Composites Science 5.10 (2021), p. 259.

[6] Ahmad Oryan et al. “Bone regenerative medicine: classic options, novel strategies, and future directions”. In: Journal of orthopaedic surgery and research 9.1 (2014), pp. 1–27.

[7] Manuel Gutierres et al. “Substitutos ósseos conceitos gerais e estado actual”. In: Arquivos de medicina 19.4 (2006), pp. 1–10.

[8] Sung Eun Kim e Kyeongsoon Park. “Recent advances of biphasic calcium phosphate bioceramics for bone tissue regeneration”. In: Biomimicked Biomaterials: Advances in Tissue Engineering and Regenerative Medicine (2020), pp. 177–188.

[9] G Daculsi et al. “Transformation of biphasic calcium phosphate ceramics in vivo: ultrastructural and physicochemical characterization”. In: Journal of biomedical materials research 23.8 (1989), pp. 883–894.

[10] Boqing Zhang et al. “3D printing of calcium phosphate bioceramic with tailored biodegradation rate for skull bone tissue reconstruction”. In: Bio-Design and Manufacturing 2 (2019), pp. 161–171.

[11] SV Dorozhkin. “Current state of bioceramics”. In: J. Ceram. Sci. Technol 9.4 (2018), pp. 353–370.

SUPPORTERS

SILVER SPONSORS

BRONZE SPONSOR

OTHER SPONSORS

ISBN: 978-972-752-312-2

www.fe.up.pt/dce
dce@fe.up.pt